Powering smart pipes with fluid flow: effect of velocity profiles

Mikail F. Lumentut[a], **Michael I. Friswell**[b, §]

[a] School of Civil and Mechanical Engineering, Curtin Institute for Computation, Curtin University, Perth, Australia

[b] College of Engineering, Swansea University, Swansea, UK

Abstract

The dynamics of elastic cantilevered smart pipes conveying fluid with non-uniform flow velocity profiles is presented for optimal power generation. The Navier-Stokes equations are used to model the incompressible flow in the circular smart pipe, and flow profile modification factors are formulated based on the Reynolds number and Darcy friction factor. The coupled constitutive dynamic equations, including the electrical circuit, are formulated for laminar and turbulent flows. Due to viscosity in a real fluid, non-uniform flow profiles induce dynamic stability and instability phenomena that affect the generated power. The system consists of an elastic pipe with segmented smart material located on the circumference and longitudinal regions, the circuit, and the electromechanical components. The modified coupled constitutive equations are solved using the weak form extended Ritz method. For faster convergence, this model is reduced from the exact solution of the pipe structure with proof mass offset. Initial validation with a uniform flow profile from previous work is conducted. With increasing flow velocity, the optimal power output and their frequency shifts are investigated both with and without the flow profile modification factors, to identify the level of instability. Further parametric studies with and without flow pulsation and base excitation are given.

Keywords: Energy harvesting; Fluid-structure interactions; Internal flow; Multi-physical system; Non-uniform flow profile; Piezoelectricity; Vibration.

1 Introduction

In this section, we provide two different types of literature review. This includes a review of the literature for the pipe conveying fluid and for the smart structure. In the vast majority of previously published works the different methods and applications have been investigated separately. In this particular context, as presented here, hybrid model interaction using these coupled systems will be the main aspect of discussion by elaborating the physical phenomena in relation to a potential application for electric power generation. The physical elements of the fluid and pipe interaction have shown interesting dynamic phenomena due to the mechanical energy transfer between these two elements. The simplest physical system has been used to understand the mathematical and experimental studies. More complicated modelling of the fluid flow in the pipe, and the ability of the flow profile to induce vibration, relies on these models, particularly for an elastic pipe which has most potential for real-life engineering applications. Examples can be found in ocean mining [1-3], oil drill-strings [4], mass-flow

§ Author to whom any correspondence should be addressed. Email: m.i.friswell@swansea.ac.uk

meters [5], water-hose [6], nano- and micro-fluidic devices [7], wave propagation due to valve closure [8], and elastic wave in submersed pipe [9].

The earliest studies of the dynamic stability and instability for pipes conveying fluid using theoretical and experimental models date back over sixty years. Starting with the work of Feodos'ev [10], the equation of motion for the flow in a pipe having both ends supported was developed. For a similar case, Housner [11] derived a different approach and proved the buckling/divergence phenomenon of pipes due to sufficiently high flow velocities. Niordson [12] derived a different theoretical model, which led to similar equations of motion and results to those obtained in [10,11]. Long [13] and Handelman [14] investigated pipes containing fluid under various conditions of end constraints to determine the effect of flow on the natural frequencies of the system. Heinrich [15] derived the dynamic equation of an infinite pipe conveying fluid under the effects of wave propagation and pressurisation. Moreover, the general equation of motion of articulated pipe systems conveying fluid using Hamilton's principle has been developed by Benjamin [16]. The experimental study with the result of the unstable oscillation or flutter of the cantilevered pipe system was also given by Benjamin [17]. Gregory and Païdoussis [18] investigated the oscillatory instabilities due to increasing flow velocity of cantilevered pipe conveying fluid using three theoretical models consisting of quasi-analytical, numerical solutions, and partial differential equations with the Galerkin method. In [16,18], the paradox of a plain cantilever pipe conveying fluid has been examined using the dynamic system to show how the mechanical energy transfer can occur between the fluid and the pipe. This indicates that the Coriolis and centrifugal forces may either stabilise or destabilise the pipe, depending on the physical phenomenon. For example, the Coriolis force has a lower effect on the first mode of the dynamic response, but has a negative damping effect to amplify the second mode of the dynamic response of the pipe. The centrifugal force using higher flow velocity causes a divergence instability (static buckling or negative stiffness instability) at the first mode. But, for the second mode, the Coriolis force using higher flow velocity overtakes the dynamic response to create a flutter instability (oscillations without bound). Thompson [19] lucidly discussed the paradox of the cantilever pipe conveying fluid using the static non-conservative system. Initially, it was called a mysterious black box. Inside the box was a hanging pipe that was a kind of inverted rigid pendulum, connected to a weight loading scale via a cable sling outside the box. If more weight was added, the scale reading increased.

Later on, pipes conveying fluid with different boundary conditions under the effects of tension, fluid pressurisation and gravitation using Newtonian mechanics were developed by Païdoussis and Issid [20]. This also includes a study of the effects of flow pulsation and parametric resonances. Laithier and Païdoussis [21] further modelled pipes conveying fluid subjected to tension and fluid gravitation and coupled the equations with Timoshenko beam theory developed using Hamiltonian mechanics. Then, the critical values for the Hopf bifurcation and the onset of chaos for a long pipe with end mass were further investigated by Modarres-Sadeghi and Païdoussis [22]. Hatfield et al. [23] developed separate analyses of the pipeline and fluid components using coupled continuity and force constraints. The effect on the velocity-dependent forces (dissipative and Coriolis forces) for the cantilevered pipe conveying fluid was further discussed by Nemat-Nasser et al. [24] where the effect of such forces may induce instability of the system. Ruta and Elishakoff [25] developed an analytical method of the sheardeformable pipe conveying fluid with a partial elastic foundation. They showed the effect of increasing critical velocity due to the increasing foundation span for the pipe using higher values of the fluid-to-pipe mass per unit length ratio. A slightly different model using a long pipe conveying fluid with elastic foundation [26] was developed to predict the criterion for the global instability of variable pipe length where it was related to the properties of the waves and boundary conditions of the pipe. The instability of long flexible pipes in water-hose applications was developed by Xie et al. [6] where they showed that the new vorticity due to the pipe wall acceleration was continuously developed and the shedding of vorticity subsequently occurs. Also, the effect of elastic wave and structural–acoustic coupling in submersed pipes was further investigated by Kalkowski et al. [9].

In addition to analytical approaches, various solution techniques have been utilized to model the fluid-pipe interaction. The spectral element method was used by Lee at al. [27] to develop the dynamic equations by considering the axial, radial, and transverse vibrations, and the equations of fluid momentum and continuity. Gorman et al. [28] developed similar system equations using the finite difference method.

Other published research works that give formulations for pipe conveying fluid using combinations of continuum mechanics and variational principles have been developed. Irchick and Holl [29] formulated Lagrange's equations using the non-material volume with fictitious particles transported into the density of momentum and kinetic energy at the control surface. An extended work with the nonlinear equations for a cantilevered pipe conveying fluid was given by Stangl et al. [30]. A slightly different technique with the non-material volume using Hamilton's principle was developed by Casetta and Pesce [31]. Upon simplification of the two methods, the reduced equation appears to be a similar form with the results comparable to those given in [16,18] and the extensive theoretical forms were further given by Païdoussis [32]. Subsequent work by De Bellis et al. [33] presented an overhanging pipe with fluid flow using compatibility, balance and deformation theory in order to formulate the equations of motion, which can be used with Euler-Bernoulli and Bresse–Timoshenko beam models. Galerkin's method with Duncan's polynomials was used to show the divergent and flutter instability of the system. Unlike the aforementioned methods, Lumentut and Friswell [34] developed the constitutive coupled equations of motion for the cantilevered smart pipe with proof mass (also called the tip or end mass in the literature) offset conveying fluid in an energy harvesting application using extended Hamiltonian mechanics with flow-charge coupling. The approach integrates the simple kinematic equation with deformation theory, linear piezoelectric beam constitutive equation-based Helmholtz free energy and circuit systems. Parametric studies were provided to analyse the effect of flutter instability with increasing flow velocity to the coupled system to generate the power output across the frequency and time domains. By reducing the equations to the mechanical system of pipe and fluid, a similar form to that of previous works in [16,18] was also obtained.

Since the coupled dynamic equations of fluid-conveying structural pipes, with embedded smart material, are proposed in this paper, it is also important to review the literature related to smart structure systems. The intrinsic properties of smart materials, such as piezoelectricity, are their capability to react to changes in the physical system such as electric, mechanical, and thermal interactions. With the attachment of smart material onto a structure, the system becomes a so-called smart structure. Smart beam and plate structures have been developed using theoretical and experimental studies for applications in structural control-based sensing and actuation systems [35,36], shape control-based sensing and actuation [37,38], feedback gain control-based sensor and actuator systems [39], and shunt control-based circuit systems [40].

Energy harvesting systems with frequency tuning have also been developed recently using various methods. In mechanical and electrical tuning systems, smart structures with the attachment of a proof mass and/or in combination with a shunt circuit, have been used to shift frequencies from high to low values in order to adapt to the vibration environment and give higher power output. These strategies have been explored using wide-ranging theoretical methods, such as circuit technique combinations [41], Rayleigh–Ritz methods [42], modal analysis methods [43], the weak-form technique [44], random vibration analysis [45,46], closed-form boundary value methods [47,48], analytical voltage- and charge-type Hamiltonian formulations [49], and electromechanical finite element analyses [50-54]. With an alternative strategy using the combination of electrical and mechanical tuning systems, others developed multiple piezoelectric bimorph beams connected electrically [55-57] and single piezoelectric beams with shunt control [44,58] in order to widen the multi-frequency band. More recently, the increasing demand to capture electrical energy using flow-induced vibrations of coupled piezoelectric or electromagnetic systems and structures [59] has yielded robust techniques. An aerodynamic system to capture electrical energy was investigated using the vortex-induced vibration of a tree-inspired system [60], transverse galloping analytical studies [61] and experimental works [62], and flapping piezoelectric flags with axial flow [63,64].

In the aforementioned works, the two independent research directions for the pipe conveying fluid and the smart structure with the mechanical and electrical tuning systems, and the fluid flow around or within the system have been presented. In this paper, we consider the non-uniform flow profile in a smart pipe with a proof mass offset, connected to a harvesting circuit interface. Some new and quite unexpected results are presented related to the physical interactions of the whole system. This paper formulates and identifies the effects of non-ideal flow within the system to induce the various possible hydro-electro-elastic stability and instability cases so as to generate the optimal power output. Initially the key formulations of each physical model are presented, but the connectivity between each is maintained. First, with the real fluid flows, the simplified Navier-Stokes equations are formulated to give the laminar and turbulent flow profiles. Second, the coupled dynamic equations of the smart pipe representing the ideal fluid, solid, circuit, and electromechanical systems are formulated using extended Hamiltonian mechanics with flow-voltage coupling. Upon establishing the flow profiles, the modified version of the coupled dynamic equations is obtained to explicitly reflect the modified formulations which depend on flow-profile modification factors. These factors have a direct relationship with Reynolds number and the Darcy friction factor. This is obviously different to the previous works in [65] who used the relationship of the multi-plug flow and CFD software (STAR-CCM) and [66] who used the relationship of the Reynolds number and the ratio of mean flow velocity and shear flow velocity. Third, a theoretical approach based on the Ritz method weak form with a four-term approximation is developed to solve the non-ideal formulations leading to the simplification of the system model with the normalised dynamic equations. Since our previous work [34] for a uniform flow velocity in smart pipe was developed using extended Hamiltonian mechanics with flow-charge coupling, we also provide the initial validation using the current method. At this stage, as shown in this paper, there are no other publications addressing the new development of the proposed studies. Finally, parametric studies focusing on the effect of the non-ideal fluid flow in the smart pipe, and to maximise the power output, are extensively discussed. These show the stability/instability analysis, the 3-D frequency response analysis, and the spatial and temporal dynamic evolutions based on varying the Reynolds number, Darcy friction factor, and flow profile modification factor. In particular, the findings also show distinctive results when using the two different smart materials for the pipe structures. In real applications, the main structure naturally excites a motion due to a surrounding vibration source. As a result, the pipe structure, mounted on it, triggers the base excitation. Also, the effect of the non-uniform flow in pipe, either with or without the existence of the flow pulsation and base excitation, is further examined.

2 Constitutive non-ideal flow-solid-circuit-electromechanical equations of smart pipe

The smart pipe system conveying fluid is shown in Fig.1a, and consists of the substructure and smart material layers. The proof mass is attached to the end of the pipe system at an offset from its centroid. The segmented system uses smart material components located at the circumference and longitudinal regions. Note that the smart material segment refers to the segments of both the piezoelectric and the thin conducting electrode components. The partial smart material segment with series electrical connection is connected with the AC-DC harvesting circuit as shown in Fig. 1b. Each time the smart pipe with fluid flow undergoes transverse vibration, the lower and upper smart material segments at the circumference region can respectively deform with tensile and compressive strains and vice versa. As a result, those segments can generate the AC electric signal. To convert to a DC electric signal, a full-bridge rectifier with the smoothing RC circuit is deployed.

We first briefly discuss the laminar and turbulent velocity profiles for incompressible flow in a circular pipe using the simplified Navier-Stokes equations. This leads to the identification of the flow profile modification factor whose value depends on the Reynolds number and the Darcy friction factor.

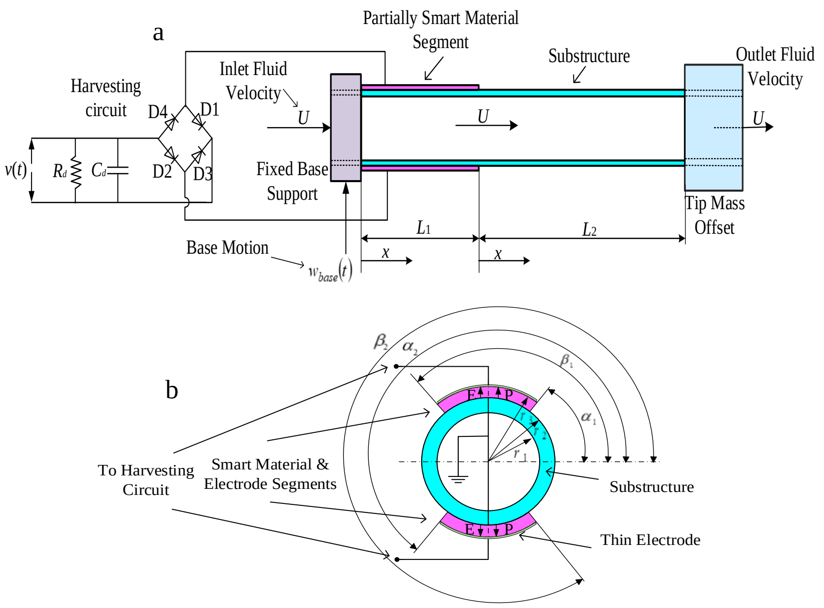

Fig. 1. Schematic of the physical system: (a) flow-conveyed smart pipe structure with proof mass offset and input base excitation connected to the circuit interface and (b) cross-section of the smart pipe with arbitrary smart material and electrode segments arranged in series connection (example).

The constitutive coupled equations of motion, with the normalised dynamic equations, are then briefly formulated to show the connections to the flow profile modification factor.

2.1. Preliminary flow profile concepts in a smart pipe

The physical coupling between the Navier-Stokes equations for laminar and turbulent flows and the constitutive smart pipe equations for the harvesting circuit enables hybrid model interaction. Thus the flow profiles affect the process of capturing the electrical energy from the mechanical motion of the smart pipe. We also notice here that the flow profile modification factor depends on both the Reynolds number and the Darcy friction factor. Without ignoring the technical connection, here the simplified exact solution of the laminar flow-based Hagen-Poiseuille equation with $\mathrm{Re}<2300$ is given, using the Navier-Stokes equations for incompressible flow in a circular pipe with variable dimensions (r,θ,x). After considering certain process conditions, the velocity profile $U=U_x$ along the pipe is a function of radial coordinate r only because we assume there is no-slip on the wall. The other two velocities, $U_r=U_\theta=0$, are defined due to the no-swirl condition. This indicates that the flow within the pipe is purely axial. Further detail of the equations can be seen in [67,68]. The remaining equations for the components (r,θ,x) can be reduced, respectively, to

$$-\frac{\partial p}{\partial r}=0\,,\quad -\frac{1}{r}\frac{\partial p}{\partial \theta}=0\,,\quad -\frac{\partial p}{\partial x}+\mu\left(\frac{\partial^2 U_x}{\partial r^2}+\frac{1}{r}\frac{\partial U_x}{\partial r}\right)=0\,. \tag{1}$$

The first two equations show that the pressure p does not vary with respect to the components (r,θ). μ is dynamic viscosity. The simplified solution is $U=U_x=-\left(r_1^2/4\mu\right)\left(\mathrm{d}p/\mathrm{d}x\right)\left(1-\left(r/r_1\right)^2\right)$. r_1 is the inner pipe radius. The average flow velocity gives,

$$\overline{U}=-\frac{1}{\pi r_1^2}\int_0^{2\pi}\int_0^{r_1}\frac{r_1^2}{4\mu}\frac{\mathrm{d}p}{\mathrm{d}x}\left(1-\left(\frac{r}{r_1}\right)^2\right)r\mathrm{d}r\mathrm{d}\theta=\frac{1}{2}U_{\max}\,, \tag{2}$$

where the maximum velocity at the centre of the pipe is $U_{\max}=-\frac{r_1^2}{4\mu}\left(\frac{\mathrm{d}p}{\mathrm{d}x}\right)=\frac{r_1^2}{4\mu}\left(\frac{\Delta p}{L}\right)$. The Hagen-Poiseuille flow profile is then given by $U=U_{\max}\left(1-\left(r/r_1\right)^2\right)$. The friction factor of the pipe $f=64/\mathrm{Re}$ can be obtained using the relations (Darcy–Weisbach equation) between the pipe head loss, obtained from the energy balance equation $\Delta p/\rho g=fL\overline{U}^2/(2Dg)$ and the average flow velocity $\overline{U}$.

The following parameters are now defined here because the interaction of the laminar flow profile and the smart structural pipe system provide modification factors if the mean/average flow velocity is used for the flow system in a smart pipe. Therefore, these parameters are used in the forthcoming section and become essential parts of the constitutive coupled equations. The flow modification factors for the four parameters can be formulated using the laminar flow velocity profile as,

$$M^fU^2=\int_0^{2\pi}\int_0^{r_1}\rho^f U_{\max}{}^2\left(1-\left(\frac{r}{r_1}\right)^2\right)^2 r\mathrm{d}r\mathrm{d}\theta=\frac{4}{3}M^f\overline{U}^2=\alpha_1^{lam}M^f\overline{U}^2\,, \tag{3.1}$$

$$I_2^fU^2=\int_0^{2\pi}\int_0^{r_1}\rho^f U_{\max}{}^2\left(1-\left(\frac{r}{r_1}\right)^2\right)^2 r^3\mathrm{d}r\mathrm{d}\theta=\frac{2}{3}I_2^f\overline{U}^2=\alpha_2^{lam}I_2^f\overline{U}^2\,, \tag{3.2}$$

$$2M^{f}U=\int_{0}^{2\pi}\int_{0}^{r_1}2\rho^{f}U_{\max}\left(1-\left(\frac{r}{r_1}\right)^{2}\right)r\mathrm{d}r\mathrm{d}\theta=2\beta_1^{lam}M^{f}\overline{U}, \tag{3.3}$$

$$2I_2^{f}U=\int_{0}^{2\pi}\int_{0}^{r_1}2\rho^{f}U_{\max}\left(1-\left(\frac{r}{r_1}\right)^{2}\right)r^{3}\mathrm{d}r\mathrm{d}\theta=\frac{4}{3}I_2^{f}\overline{U}=2\beta_2^{lam}I_2^{f}\overline{U}. \tag{3.4}$$

M^{f} and I_2^{f} are the mass of fluid per unit length and the mass moment of inertia of fluid, respectively. The two flow profile modification factors $\alpha_1^{lam}=4/3$ and $\beta_1^{lam}=1$ are similar to the results given in [66]. The other two factors $\alpha_2^{lam}=2/3$ and $\beta_2^{lam}=2/3$ are new, and are significant if the fluid rotary inertia is taken into account. Eq. (3.1) has a direct relevance to the momentum correction factor developed by Streeter [69]. It is noted that the fluid moment inertia I_2^{f} implied by Eq. (3.2) is based on the kinetic energy of the fluid element inside the pipe. This occurs due to the rotation of the element of pipe itself, caused by transverse bending vibration as a result of fluid flow. The calculation of fluid rotary inertia is nothing to do with the swirl flow itself. But, it may be that if the swirl flow is considered in the flexible pipe, the physical and mathematical insights for fluid rotary inertia can be better understood for the pipe conveying fluid.

For turbulent flow in a pipe with $\mathrm{Re}>2300$, the components of velocity, shear stress, pressure and other variables occur as random fluctuations in time and space. For example, the flow velocity components U_x, U_r, U_θ in a pipe correspond to the *x*, *r*, and θ directions. Initially, the time-average turbulent and fluctuating velocities along the pipe can be defined as $U_x=\bar{u}_x+u'_x$ where the related time average of velocity is $\bar{u}_x=(1/T)\left(\int_0^T U_x\mathrm{d}t\right)$ and the average of fluctuating velocity is defined as $\overline{u'_x}=(1/T)\left(\int_0^T\left(U_x-\bar{u}_x\right)\mathrm{d}t\right)=0$. However, the mean square of the fluctuating velocity is given as $\overline{u'^2_x}=(1/T)\left(\int_0^T u'^2_x\mathrm{d}t\right)\neq 0$. Similarly, the remaining velocities U_r, U_θ can also be defined using time average procedures. After substituting all time-average quantities into the Navier-Stokes equations for incompressible flow in the circular pipe equations, the result can be further simplified to give the modified Navier-Stokes equation in the *x* direction along the pipe in terms of time-average velocities [67,68]. Without showing the details of the derivation here, the modified equation will include the additional parameters $\rho\overline{u'^2_x}$, $\rho\overline{u'_x}\overline{u'_r}$ and $\rho\overline{u'_x}\overline{u'_\theta}$ (turbulent stresses or Reynolds stresses). In White [67] and Durst [68], however, the parameter $\rho\overline{u'_x}\overline{u'_r}$ along with the boundary layer flow at the radial coordinate *r* to the wall is dominant where it is relevant to the flow within the pipe in *x* direction. As a result, the von Karman-Prandtl equation can be determined to give the universal logarithmic law of the velocity close to the wall. Similar to the laminar equation, the turbulent flow equation based on the time-average equation can be reduced to,

$$-\frac{\partial p}{\partial x}-\frac{1}{r}\frac{\partial\left(r\bar{\tau}_{rx}\right)}{\partial r}=0, \tag{4}$$

where the total fluid shear stress is $\bar{\tau}_{rx}=\mu\left(\mathrm{d}\bar{u}_x/\mathrm{d}r\right)-\rho\overline{u'_x}\overline{u'_r}=\bar{\tau}_{rx}^{lam}+\bar{\tau}_{rx}^{turb}$. The turbulent shear stress can also be stated as $\bar{\tau}_{rx}^{turb}=\rho\ell^2\left(\mathrm{d}\bar{u}_x/\mathrm{d}\bar{z}\right)^2\approx\mu_t\,\mathrm{d}\bar{u}_x/\mathrm{d}\bar{z}$ where $\mu_t=\rho\ell^2\left|\mathrm{d}\bar{u}_x/\mathrm{d}\bar{z}\right|$ is the eddy viscosity of the bundles of fluid particles over certain a mixing length $\ell = k\hat{z}$. This mixing length defines the distance of a particle travelling with another at a different velocity in the turbulent flow profile. *k* is a von Karman constant and independent variable $\hat{z}$ is measured from the wall as opposed to radial coordinate *r*, which is measured from the pipe centerline. If the second term of the turbulent shear stress is zero, the equation will be similar to laminar flow. Further modification of Eq. (4) gives $\bar{\tau}_{rx} = \bar{\tau}_{rx}^{lam} + \bar{\tau}_{rx}^{turb} == \tau_w\left(1-\hat{z}/r_1\right)$. $\tau_w = -\left(r_1/2\right)\left(\mathrm{d}p/\mathrm{d}x\right)$ is the wall shear stress for fluid flow. For turbulent flow $\bar{\tau}_{rx}^{lam} << \bar{\tau}_{rx}^{turb}$. Therefore, we obtain $\mathrm{d}\bar{u}_x/\mathrm{d}\hat{z} == \pm\sqrt{\tau_w/\rho}\left(1/k\hat{z}\right) = u^*/k\hat{z}$. After simplification, the von Karman-Prandtl equation for the turbulent region at the overlap layer velocity can be reduced to give $\bar{u}_x/u^* = \left(1/k\right)\ln\left(\hat{z}/z_b\right) + \bar{u}_{zb}/u^*$. At the edge of the buffer layer z_b of the turbulent flow, the velocity can be defined as $\bar{u}_{zb}$. This clearly implies a logarithmic velocity distribution [67] that can be expressed as,

$$\frac{\bar{u}_x}{u^*} = \frac{1}{k}\ln\left(\frac{\hat{z}u^*}{\upsilon}\right) + B. \tag{5}$$

Parameters *k* and *B* are universal constants for turbulent flow and υ is fluid kinematic viscosity. For a smooth-walled pipe, Coles and Hirst [70] suggested the values of $k = 0.41$ and $B = 5.0$. For a rough-walled pipe, Eq. (5) can be further reduced using $\Delta B \approx \left(1/k\right)\ln\left(1 + 0.3u^*\delta/\upsilon\right)$ resulting in a down shift of the logarithmic overlap velocity profile. ΔB is the parameter of sand-grain roughness. δ is the roughness height that depends on the particular material and the condition of the pipe. The modified logarithmic equation for a rough-walled pipe is then $\bar{u}_x/u^* = \left(1/k\right)\ln\left(\dfrac{\hat{z}u^*/\upsilon}{1+0.3u^*\delta/\upsilon}\right) + B$. Further detail can be seen in [67]. In this case, the average flow velocity for a rough-walled pipe can be formulated to give,

$$\bar{U} = \frac{1}{\pi r_1^2}\int_0^{2\pi}\int_0^{r_1}\bar{u}_x r\mathrm{d}r\mathrm{d}\theta = u^*\left(\frac{1}{k}\ln\left(\frac{\dfrac{r_1u^*}{\upsilon}}{10+3\delta\dfrac{u^*}{\upsilon}}\right) + B + \frac{683}{851k}\right). \tag{6}$$

The related expressions below can be determined as,

$$\frac{\bar{U}}{u^*} = \sqrt{\frac{\rho\bar{U}^2}{\tau_w}} = \sqrt{\frac{8}{f}} \quad , \quad \frac{r_1u^*}{\upsilon} = \frac{1}{2}\mathrm{Re}\sqrt{\frac{f}{8}}. \tag{7}$$

For a smooth-walled pipe, the average flow velocity is formulated as,

$$\bar{U} = \frac{1}{\pi r_1^2}\int_0^{2\pi}\int_0^{r_1}\bar{u}_x r\mathrm{d}r\mathrm{d}\theta = u^*\left(\frac{1}{k}\ln\left(\frac{r_1u^*}{\upsilon}\right) + B - \frac{3}{2k}\right). \tag{8}$$

Eq. (8) can be modified using the Darcy friction factor *f* and the Reynolds number Re [67] given by,

$$\frac{1}{\sqrt{f}} = \frac{1}{\sqrt{8}}\left(\frac{1}{k}\ln\left(\mathrm{Re}\sqrt{f}\right) + \frac{1}{k}\ln\left(\frac{\sqrt{2}}{8}\right) + B - \frac{3}{2k}\right). \tag{9}$$

Note that Eq. (9) can be solved, although it is often implicit, especially for solving *f*. For a rough-walled pipe, the approximation of the friction factor can be formulated to give an implicit formula with greater calculation. However, the Colebrook–White equation based on an interpolation provides a simpler implicit formula, different from the reduced equation using Eq. (9). Since the implicit formula is still quite tedious, modifying the formulas into an explicit form for a rough-wall pipe can be an alternative and direct solution. One popular example of an explicit formula was given by Haaland [71] by intuitively combining the Prandtl, von Karman, and Colebrook–White formulas. Note that we do not focus here on the details of finding the explicit correlation because one of the main aspects of this paper is to investigate the connectivity between the flow profile parameters and the pipe parametric equations that potentially affect the electromechanical system of the energy harvester. As an example, the following equations related to the mean/average flow velocity and flow modification factors for a smooth-wall turbulent pipe flow are given as,

$$M^f U^2 = \int_0^{2\pi}\int_0^{r_1} \rho^f \bar{u}_x^{\,2} r\,\mathrm{d}r\,\mathrm{d}\theta = M^f u^{*2}\left(\frac{1}{2k^2}\left(2\ln\left(\frac{r_1u^*}{\upsilon}\right)^2 - 6\ln\left(\frac{r_1u^*}{\upsilon}\right)+7\right)+\frac{B}{k}\left(2\ln\left(\frac{r_1u^*}{\upsilon}\right)-3\right)+B^2\right)$$

$$= M^f\bar{U}^2\frac{f}{8k^2}\left(\ln\left(\frac{\sqrt{2}}{8}\mathrm{Re}\sqrt{f}\right)^2+(2Bk-3)\ln\left(\frac{\sqrt{2}}{8}\mathrm{Re}\sqrt{f}\right)+3.5-3Bk+B^2k^2\right)=\alpha_1^{turb}M^f\bar{U}^2 \quad , \qquad (10.1)$$

$$I_2^f U^2 = \int_0^{2\pi}\int_0^{r_1} \rho^f \bar{u}_x^{\,2} r^3\,\mathrm{d}r\,\mathrm{d}\theta = I_2^f u^{*2}\left(\frac{2}{144k^2}\left(72\ln\left(\frac{r_1u^*}{\upsilon}\right)^2 - 300\ln\left(\frac{r_1u^*}{\upsilon}\right)+415\right)+\frac{B}{6k}\left(12\ln\left(\frac{r_1u^*}{\upsilon}\right)-25\right)+B^2\right)$$

$$= I_2^f\bar{U}^2\frac{f}{8k^2}\left(\ln\left(\frac{\sqrt{2}}{8}\mathrm{Re}\sqrt{f}\right)^2+\frac{12Bk-25}{6}\ln\left(\frac{\sqrt{2}}{8}\mathrm{Re}\sqrt{f}\right)+\frac{415}{72}-\frac{25Bk}{6}+B^2k^2\right)=\alpha_2^{turb}I_2^f\bar{U}^2 , \qquad (10.2)$$

$$2M^f U = \int_0^{2\pi}\int_0^{r_1} 2\rho^f \bar{u}_x\, r\,\mathrm{d}r\,\mathrm{d}\theta = 2M^f u^*\left(\frac{1}{k}\ln\left(\frac{r_1u^*}{\upsilon}\right)+B-\frac{3}{2k}\right)=2M^f\bar{U}=2\beta_1^{turb}M^f\bar{U} \quad , \qquad (10.3)$$

$$2I_2^f U = \int_0^{2\pi}\int_0^{r_1} 2\rho^f \bar{u}_x r^3\,\mathrm{d}r\,\mathrm{d}\theta = 2I_2^f\bar{U}\left(\frac{1}{2k}\left(\frac{r_1u^*}{\upsilon}\right)+\frac{B}{2}-\frac{25}{24k}\right)$$

$$= 2I_2^f\bar{U}\sqrt{\frac{f}{8}}\left(\frac{1}{2k}\ln\left(\frac{\sqrt{2}}{8}\mathrm{Re}\sqrt{f}\right)+\frac{B}{2}-\frac{25}{24k}\right)=2\beta_2^{turb}I_2^f\bar{U} . \qquad (10.4)$$

The turbulent flow profile modification factors $\alpha_1^{turb}, \alpha_2^{turb}, \beta_1^{turb}, \beta_2^{turb}$ from Eqs. (10a)-(10d) rely on the parameters of the Darcy friction factor and Reynolds number. These factors can be calculated by combining with Eq. (9).

2.2. *Hamiltonian mechanics with flow-voltage coupling*

The uniform flow profile in cantilevered smart pipe is developed using extended Hamiltonian mechanics with flow-voltage coupling. It presents the functional forms of the coupled system of the fluid, solid, circuit, and electromechanical components. The system here can be categorised as a smart pipe conveying fluid with a segmented piezoelectric element and a harvesting circuit interface. Note that the following equations are different to those given in [34] as they emphasised a uniform flow profile for the smart pipe with the segmented electrodes using extended Hamiltonian mechanics with flow-charge coupling.

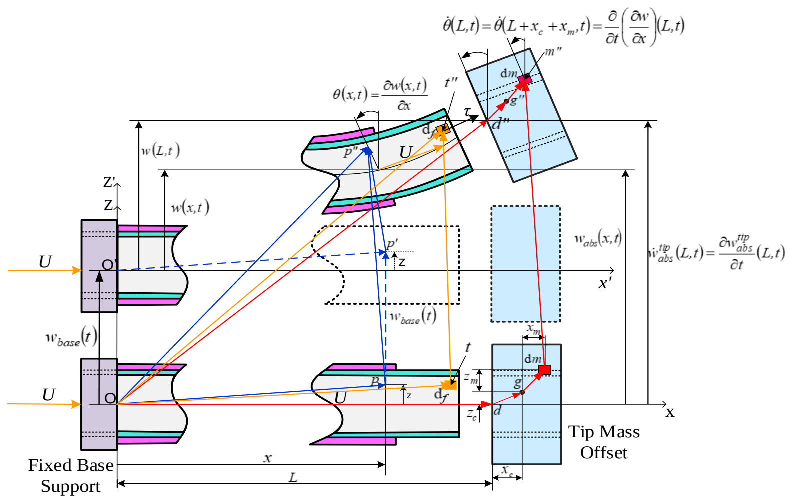

Fig.2 Dynamic motions of the smart pipe structure with proof mass offset under fluid

As shown in Fig 2, the smart pipe appears to undergo dynamic motion due to the fluid flowing with a steady flow velocity U relative to the pipe itself. Since the fluid continuously flows through the smart pipe, its motion can be traced analytically using the kinematic equations based on the position vector forms from the fixed reference frame of oXZ to the initial reference frame of $o'XZ$. Since the fluid element in the smart pipe has a reference configuration at control volume and surface, the system around the pipe region obviously undergoes the rate of change of physical property. This is related to the material derivative from the continuum body and Reynolds transport theorem. The pipe here is not a rigid structure. Therefore, its motions at any instant of time undergoes a bending deformation. On the other hand, the proof mass is a rigid structure, but its motions obviously depend on the dynamics of the tip. It is important to note here that details of the kinematic equations of the elemental fluid and pipe structure were given by Lumentut and Friswell [34] and can be essentially used here to develop the following equations.

The simplified equation of motion using the Hamiltonian method with flow-voltage coupling can be stated as,

$$\int_{t_1}^{t_2} \delta\left(L_a + W_f\right)\mathrm{d}t = 0 \quad \left.\begin{matrix} L_a \in \left\{KE, H, PE^{sub}\right\} \\ W_f \in \left\{WF_D, WF\right\} \end{matrix}\right\} , \tag{11}$$

$$\text{or} \quad \int_{t_1}^{t_2} \left(\delta KE - \delta H - \delta PE^{subs} + \delta WF + \delta WF_D\right)\mathrm{d}t = 0 . \tag{12}$$

The functional energy form given in Eq. (12) represents the parameters for kinetic energy KE, electrical enthalpy of piezoelectricity H, substructure strain energy PE^{sub}, non-conservative work WF due to base excitation and electrical output, and the energy gained due to fluid flow WF_D. Here, the kinetic energy consisting of the solid system (the smart pipe and proof mass offset) and fluid flow along the two segments of the system can be formulated after simplification as,

$$KE = \frac{1}{2}\int_0^{L_1}\int_{A^{(1)}} \rho^{(1)} \dot{\boldsymbol{R}}^{pp''} \cdot \dot{\boldsymbol{R}}^{pp''} \,\mathrm{d}A^{(1)}\,\mathrm{d}x + \frac{1}{2}\int_0^{L_1}\int_{A^{(2)}} \rho^{(2)} \dot{\boldsymbol{R}}^{pp''} \cdot \dot{\boldsymbol{R}}^{pp''} \,\mathrm{d}A^{(2)}\,\mathrm{d}x$$

$$+ \frac{1}{2}\int_0^{L_2}\int_{A^{(1)}} \rho^{(1)} \dot{\boldsymbol{R}}^{pp''} \cdot \dot{\boldsymbol{R}}^{pp''} \,\mathrm{d}A^{(1)}\,\mathrm{d}x + \frac{1}{2}\int_0^{L^{tip}}\int_{A^{tip}} \rho^{tip} \dot{\boldsymbol{R}}^{mm''} \cdot \dot{\boldsymbol{R}}^{mm''} \,\mathrm{d}A^{tip}\,\mathrm{d}x_{tip}$$

$$+\frac{1}{2}\int_{0}^{L_1}\int_{A^f}\rho^f \boldsymbol{v}^f(t)\cdot\boldsymbol{v}^f(t)\,\mathrm{d}A^f\,\mathrm{d}x+\frac{1}{2}\int_{0}^{L_2}\int_{A^f}\rho^f \boldsymbol{v}^f(t)\cdot\boldsymbol{v}^f(t)\,\mathrm{d}A^f\,\mathrm{d}x\,. \tag{13}$$

Parameters $\rho^{(1)},\rho^{(2)},\rho^{tip}$ and ρ^f represent the mass densities of the substructure, the piezoelectric, the proof mass offset, and the fluid components, respectively. The fluid element flowing within the pipe can be formulated using Reynolds transport theorem and the material derivative as,

$$\frac{\mathrm{D}\boldsymbol{R}}{\mathrm{D}t}\equiv\boldsymbol{v}^f(t)=\left(\frac{\partial\boldsymbol{R}^{pp''}}{\partial t}+U\frac{\partial\boldsymbol{R}^{pp''}}{\partial x}\right), \tag{14}$$

where $\mathrm{D}\boldsymbol{R}/\mathrm{D}t$ is the material derivative of the fluid element. The position vector $\boldsymbol{R}^{pp''}$, as shown in Fig. 2, can be specified as the moving structure and fluid elements from initial to final positions as,

$$\boldsymbol{R}^{pp''}(x,z,t)=-z\sin\theta(x,t)\boldsymbol{e}_1+\left(w_{base}(t)+w(x,t)\right)\boldsymbol{e}_3\,. \tag{15}$$

The velocity of the elemental proof mass offset can also be formulated as,

$$\begin{aligned}\dot{\boldsymbol{R}}^{mm''}(L,z,t)&=\dot{\boldsymbol{R}}^{od''}+\dot{\boldsymbol{R}}^{d''g''}+\dot{\boldsymbol{R}}^{g''m''}-\dot{\boldsymbol{R}}^{od}-\dot{\boldsymbol{R}}^{dg}-\dot{\boldsymbol{R}}^{gm}\\&=\left(\dot{w}_{base}(t)+\dot{w}(L,t)\right)\boldsymbol{e}_3-\dot{\theta}(L,t)\boldsymbol{e}_2\times\left(z_c\,\boldsymbol{e}_3+x_c\,\boldsymbol{e}_1\right)-\dot{\theta}(L,t)\boldsymbol{e}_2\times\left(z_m\,\boldsymbol{e}_3+x_m\,\boldsymbol{e}_1\right).\end{aligned} \tag{16}$$

Note that detailed derivations and explanations of the elemental fluid and structure in the vector forms can be found in [34]. Eq. (13) can be reformulated after manipulation and simplification as,

$$\begin{aligned}\int_{t_1}^{t_2}\delta KE=\int_{t_1}^{t_2}\Bigg\{&\int_0^L\Bigg(\left(\sum_{h=1}^{2}G_h(\gamma)H_1(x)I_{21}+H_2(x)I_{22}\right)\dot{\theta}(x,t)\delta\dot{\theta}(x,t)+\left(\sum_{h=1}^{2}G_h(\gamma)H_1(x)I_{01}+H_2(x)I_{02}\right)\dot{w}(x,t)\delta\dot{w}(x,t)\Bigg)\mathrm{d}x\\&+H_2(x)\left(I_0^{tip}\dot{w}(L_2,t)\delta\dot{w}(L_2,t)+I_2^{tip}\dot{\theta}(L_2,t)\delta\dot{\theta}(L_2,t)+I_0^{tip}x_c\left(\dot{w}(L_2,t)\delta\dot{\theta}(L_2,t)+\delta\dot{w}(L_2,t)\dot{\theta}(L_2,t)\right)\right)\\&+\int_0^L\int_{A^f}\sum_{n=1}^{2}H_n(x)\Bigg(\rho^f\left(\dot{w}(x,t)\delta\dot{w}(x,t)+z^2\dot{\theta}(x,t)\delta\dot{\theta}(x,t)+\dot{w}_{base}(t)\delta\dot{w}(x,t)\right)\\&-\rho^f U\left(2z^2\frac{\partial\dot{\theta}(x,t)}{\partial x}\delta\theta(x,t)+2\frac{\partial\dot{w}(x,t)}{\partial x}\delta w(x,t)\right)\\&+\rho^f U^2\left(\frac{\partial w(x,t)}{\partial x}\delta\frac{\partial w(x,t)}{\partial x}+z^2\frac{\partial\theta(x,t)}{\partial x}\delta\frac{\partial\theta(x,t)}{\partial x}\right)\Bigg)\mathrm{d}A^f\,\mathrm{d}x\\&+\int_{A^f}\rho^f UH_2(x)\left(z^2\dot{\theta}(L_2,t)\delta\theta(L_2,t)+\dot{w}(L,t)\delta w(L_2,t)+\dot{w}_{base}(t)\delta w(L_2,t)\right)\mathrm{d}A^f\Bigg\}\mathrm{d}t\quad.\end{aligned} \tag{17}$$

Note that the physical geometry in Fig. 1 has different mode shapes along the x-axis due to having the two segments. Hence, the Heaviside functions of the pipe, $H_1(x)=H(x)-H(x-L_1)$ and $H_2(x)=H(x)-H(x-L_2)$, on the axial region are introduced. The Heaviside functions for the two segmented smart material components $G_1(\gamma)=H(\gamma-\alpha_1)-H(\gamma-\beta_1)$ and $G_2(\gamma)=H(\gamma-\alpha_2)-H(\gamma-\beta_2)$ on the layer of the circumference region at the polar coordinate system are also introduced. Therefore, Eq. (17) is slightly different to the given formulas in [34] in which two segmented electrodes were used. However, changing this formulation into that for the segmented electrodes is not difficult by dropping $G_h(\gamma)$ from Eq. (17). Note that since the electrode is very thin (in nano scale) compared with the piezoelectric component, its stiffness and mass moments of inertia can be ignored. Parameters I_{0n} and I_{2n} represent the zeroth and second mass moments of inertia of the segmented structures whereas parameters I_0^{tip} and I_2^{tip} represent the zeroth and second mass moments of the proof mass. Also note that details of the mathematical expressions for the proof mass offset as shown in the fifth-eighth terms of Eq. (17) can be found in [51]. They were reduced since the relative displacement $w(x,t)$ is defined as the difference between the absolute displacement $w_{abs}(x,t)$ and the base excitation $w_{base}(t)$.

The electrical enthalpy of the piezoelectric material in tensor notation is formulated according to continuum thermodynamics. For simplification, it can be condensed using Voigt's notation and then further reduced using Einstein's summation convention [72,73] as,

$$H\left(S_1^{(2)},E_3^{(2)}\right)=\frac{1}{2}\bar{c}_{11}^{(2,E)}S_1^{(2)2}-e_{31}^{(2)}S_1^{(2)}E_3^{(2)}-\frac{1}{2}\,\varepsilon_{33}^{(2,S)}E_3^{(2)2}\,. \tag{18.1}$$

where $\varepsilon_{33}^{(2,S)}=\varepsilon_{33}^{(2,T)}-d_{31}^2\bar{c}_{11}^{(2,E)},\ e_{31}=d_{31}\bar{c}_{11}^{E},\ E_3=-\nabla\varphi(r,t)=-v(t)\left(\mathrm{d}\,\vartheta(r)/\mathrm{d}\,r\right),$ (18.2)

$$\vartheta(r,t)=z_\theta\,\mathrm{r}_3\Big/\int_\alpha^\beta\int_{\mathrm{r}_2}^{\mathrm{r}_3}r\mathrm{d}r\mathrm{d}\gamma\ \approx r\,\mathrm{r}_3\Big/\int_{\mathrm{r}_2}^{\mathrm{r}_3}r\mathrm{d}r\quad \text{if}\ z_\theta=r(\beta-\alpha)\,\forall\,\alpha\in\{\alpha_1,\alpha_2\}\ \text{and}\ \beta\in\{\beta_1,\beta_2\}\ . \tag{18.3}$$

The general parameters $\bar{c}^E$, $\bar{e}$, $\bar{\varepsilon}^S$, E, T, and S represent the piezoelectric elastic stiffness at constant electric field, piezoelectric coefficient, permittivity under constant strain, electric field, stress, and strain, respectively. Note that Eqs. (18.1)-(18.3) are clearly different to the equations given in [34]. The general strain field $S_1(x,t)=-\,z\,\partial^2 w(x,t)/\partial x^2$ can be used for each layer and the substructure stress can be stated as $T_1^{(1)}=\bar{c}_{11}^{(1)}S_1^{(1)}$. The variational form of the electrical enthalpy in Eq. (18.1) can be formulated as,

$$\delta H\left(S_1^{(2)},E_3^{(2)}\right)=\int_0^{L_1}\int_{A^{(2)}}\left(\frac{\partial H}{\partial S_1^{(2)}}\delta S_1^{(2)}-\frac{\partial H}{\partial E_3^{(2)}}\delta E_3^{(2)}\right)\mathrm{d}A^{(2)}\mathrm{d}x\,\cdot \tag{19.1}$$

where $\frac{\partial H}{\partial S_1^{(2)}}\delta S_1^{(2)}=\left(\bar{c}_{11}^{(2,E)}S_1^{(2)}-e_{31}E_3\right)\delta S_1^{(2)}$, $\frac{\partial H}{\partial E_3^{(2)}}\delta E_3^{(2)}=\left(\mathrm{e}_{31}^{(2)}S_1^{(2)}+\varepsilon_{33}^{(2,S)}E_3^{(2)}\right)\delta E_3^{(2)}$. (19.2)

Eq. (19.1) can be further extended in terms of the functional form between two specified times as,

$$\int_{t_1}^{t_2}\delta H\mathrm{d}t=\int_{t_1}^{t_2}\left\{\int_0^L\left(\sum_{h=1}^{2}G_h(\gamma)H_1(x)C_{t1}^{(2)}\right)\frac{\partial^2 w(x,t)}{\partial x^2}\delta\frac{\partial^2 w(x,t)}{\partial x^2}\mathrm{d}x+\int_0^L\int_{A^{(2)}}\sum_{h=1}^{2}ze_{31}^{(2)}E_3^{(2)}G_h(\gamma)H_1(x)\delta\frac{\partial^2 w(x,t)}{\partial x^2}\mathrm{d}A^{(2)}\mathrm{d}x\right.$$

$$\left.-\int_0^L\int_{A^{(2)}}\sum_{h=1}^{2}\left(-ze_{31}^{(2)}\frac{\partial^2 w(x,t)}{\partial x^2}+\varepsilon_{33}^{(2,S)}E_3^{(2)}\right)G_h(\gamma)H_1(x)\delta E_3^{(2)}\mathrm{d}A^{(2)}\mathrm{d}x\right\}\mathrm{d}\,t\,. \tag{20}$$

Parameter $C_{t1}^{(2)}$ represents the stiffness coefficient of the first segment for the smart material layer. Note that the Heaviside functions $G_h(\gamma)$ for the two segmented smart material components were used for different stiffnesses and electrical outputs located at the upper and lower regions of circumference for the smart pipe. If the system with two segmented electrodes was chosen, only $G_h(\gamma)$ located in the first part of Eq. (20) for the stiffness parameter can be neglected. The variational form of potential energy or strain energy of the two segmented substructure can be formulated as,

$$\delta PE^{subs}=\int_0^{L_1}\int_{A^{(1)}}T_1^{(1)}\delta S_1^{(1)}\mathrm{d}A^{(1)}\mathrm{d}x+\int_0^{L_2}\int_{A^{(1)}}T_1^{(1)}\delta S_1^{(1)}\mathrm{d}A^{(1)}\mathrm{d}x\quad . \tag{21}$$

or reformulated to give,

$$\int_{t_1}^{t_2} \delta PE^{subs}\,\mathrm{d}t = \int_{t_1}^{t_2} \left\{ \int_0^L \left(H_1(x) C_{t1}^{(1)} + H_2(x) C_{t2}^{(1)} \right) \frac{\partial^2 w(x,t)}{\partial x^2} \delta \frac{\partial^2 w(x,t)}{\partial x^2} \mathrm{d}x \right\} \mathrm{d}t \,. \tag{22}$$

Parameters $C_{t1}^{(1)}$ and $C_{t2}^{(1)}$ represent the stiffness coefficients of the first and second segments for the substructures layer and they depend on the geometry of the pipe itself without the smart material properties. In essence, Eq. (20) implies the inclusion of the strain energy of the smart material as it is one of the parts of the continuum thermodynamics. Therefore, it was excluded in Eq. (22). The Heaviside functions $H_1(x)$ and $H_2(x)$ are introduced to the first and second segments of the pipe on the x-axis region. Note that Eq. (22) is different to the formula given in [34].

The non-conservative work on the system related to the input base excitation and electrical outputs can be stated as,

$$\int_{t_1}^{t_2} \delta WF \mathrm{d}t = \int_{t_1}^{t_2} \left\{ \left(-\int_0^L \left(\sum_{h=1}^{2} G_h(\gamma) H_1(x) I_{01} + H_2(x) I_{02} \right) \delta w(x,t) \mathrm{d}x - I_0^{tip} x_c H_2(x) \delta\theta(L_2,t) - I_0^{tip} H_2(x) \delta w(L_2,t) \right) \ddot{w}_{base}(t) \right.$$

$$\left. + q_{11}(t)\delta v_{11}(t) + q_{12}(t)\delta v_{12}(t) \right\} \mathrm{d}t \,. \tag{23}$$

It is noted here that Eq. (23) is again different to the formula given in [34].

The variational form of energy gained due to fluid flow at the free end of the pipe can be formulated as,

$$\int_{t_1}^{t_2} \delta WF_D \,\mathrm{d}t = \int_{t_1}^{t_2} \left\{ -M^f U \left(\frac{\partial \boldsymbol{R}^{tt''}}{\partial t} + U \boldsymbol{\tau} \right) \cdot \delta \boldsymbol{R}^{tt''} \right\} \mathrm{d}t \;\;. \tag{24}$$

The unit vector tangent to a fluid element in the pipe and the position vector $\boldsymbol{R}^{tt''}$ as shown in Fig. 2 is given by,

$$\boldsymbol{\tau} = \frac{\partial (z\theta(L,t))}{\partial x} \boldsymbol{e}_1 + \theta(L,t) \boldsymbol{e}_3 \,, \quad \boldsymbol{R}^{tt''}(L,z,t) = \boldsymbol{R}^{od''} - \boldsymbol{R}^{ot} = -z\theta(L,t)\boldsymbol{e}_1 + \left(w_{base}(t) + w(L,t) \right) \boldsymbol{e}_3 \,. \tag{25}$$

Since Eq. (25) with $WF_D \neq 0$ is a non-conservative system due to the discharged fluid, it implies two conditions of the system. If U is positive and sufficiently small, $WF_D < 0$ may occur when the first term of the multiplication inside the curly brackets is more dominant than the second part due to the Coriolis force. Thus, the free motion of the pipe is damped. If U is positive and sufficiently large, $WF_D > 0$ may occur when the second term has the opposite sign during a cycle of oscillation. As a result, free motion of the cantilevered pipe is amplified since the fluid feeds energy into the pipe. In such a situation, dynamic instability of the pipe occurs performing a dragging and lagging motion that has been demonstrated in experimental and theoretical studies [16,18] After manipulation and simplification, Eq. (24) can be reformulated using Eq. (25), giving,

$$\int_{t_1}^{t_2} \delta WF_D \,\mathrm{d}t = -\int_{t_1}^{t_2} \left\{ \int_{A^f} \rho^f U H_2(x) \left(z^2 \dot{\theta}(L_2,t) \delta\theta(L_2,t) + \dot{w}_{base}(t) \delta w(L_2,t) + \dot{w}(L_2,t) \delta w(L_2,t) \right) \mathrm{d}A^f \right.$$

$$- \rho^f U^2 \int_0^L \int_{A^f} \sum_{n=1}^{2} H_n(x) \left(\frac{\partial (z\theta(x,t))}{\partial x} \delta \frac{\partial (z\theta(x,t))}{\partial x} + \theta(x,t) \delta\theta(x,t) \right) \mathrm{d}A^f \,\mathrm{d}x$$

$$\left. - \int_0^L \sum_{n=1}^{2} H_2(x) \left(I_2^f U^2 \frac{\partial^2 \theta(x,t)}{\partial x^2} \delta\theta(x,t) + M^f U^2 \frac{\partial \theta(x,t)}{\partial x} \delta w(x,t) \right) \mathrm{d}x \right\} \mathrm{d}t \,. \tag{26}$$

The variational operations can be used in the functional energy forms in Eq. (12) associated with Eqs. (17), (20), (22), (23) and (26) representing the continuous differentiable functions of virtual displacements, electric field and voltages for the whole system. These can be stated as,

$$L_a = L_a \begin{pmatrix} \dot{w}(x,t),\ \dot{w}(L_2,t)\ , \dfrac{\partial \dot{w}(x,t)}{\partial x}, \dfrac{\partial \dot{w}(L_2,t)}{\partial x}, w(x,t), w(L_2,t), \\ \dfrac{\partial w(x,t)}{\partial x}, \dfrac{\partial w(L_2,t)}{\partial x}, \dfrac{\partial^2 w(x,t)}{\partial x^2}, E_3^{(2)}(r,t) \end{pmatrix}, \tag{27.1}$$

$$W_f = W_f \left(w(x,t), \frac{\partial w(L_2,t)}{\partial x}, w(L_2,t), \frac{\partial w(x,t)}{\partial x}, \frac{\partial^2 w(x,t)}{\partial x^2}, v_{11}(t), v_{12}(t) \right) \quad . \tag{27.2}$$

Equations (27.1) and (27.2) can be further formulated using total differential equations as,

$$\delta L_a = \overbrace{\frac{\partial L_a}{\partial \dot{w}(x,t)} \delta \dot{w}(x,t) + \frac{\partial L_a}{\partial \dot{w}(L_2,t)} \delta \dot{w}(L_2,t) + \frac{\partial L_a}{\partial\left(\dfrac{\partial \dot{w}}{\partial x}(x,t)\right)} \delta\left(\frac{\partial \dot{w}}{\partial x}(x,t)\right) + \frac{\partial L_a}{\partial\left(\dfrac{\partial \dot{w}}{\partial x}(L_2,t)\right)} \delta\left(\frac{\partial \dot{w}}{\partial x}(L_2,t)\right)}^{\text{Virtual kinetic energy based on generalised velocities of the solid, fluid, and proof mass offset}}$$

$$\overbrace{+ \frac{\partial L_a}{\partial w(x,t)} \delta w(x,t) + \frac{\partial L_a}{\partial w(L_2,t)} \delta w(L_2,t) + \frac{\partial L_a}{\partial\left(\dfrac{\partial w(x,t)}{\partial x}\right)} \delta\left(\frac{\partial w(x,t)}{\partial x}\right) + \frac{\partial L_a}{\partial\left(\dfrac{\partial w(L_2,t)}{\partial x}\right)} \delta\left(\frac{\partial w(L_2,t)}{\partial x}\right)}^{\text{Virtual kinetic energy based on generalised velocities of the solid and fluid}}$$

$$+ \overbrace{\frac{\partial L_a}{\partial\left(\dfrac{\partial^2 w(x,t)}{\partial x^2}\right)} \delta\left(\frac{\partial^2 w(x,t)}{\partial x^2}\right)}^{\text{Virtual kinetic energy based on generalised velocities of the solid and fluid and virtual potential energy based on generalised mechanical strain}} + \overbrace{\frac{\partial L_a}{\partial E_3^{(2)}(r,t)} \delta E_3^{(2)}(r,t)}^{\text{Virtual electrical energy based on electric field}}, \tag{28.1}$$

$$\delta W_f = \overbrace{\frac{\partial W_f}{\partial w(x,t)} \delta w(x,t) + \frac{\partial W_f}{\partial\left(\dfrac{\partial w}{\partial x}(L,t)\right)} \delta\left(\frac{\partial w}{\partial x}(L,t)\right) + \frac{\partial W_f}{\partial w(L,t)} \delta w(L,t)}^{\text{Virtual energy gained due to fluid and virtual work based on generalised displacement and proof mass offset}}$$

$$\overbrace{+ \frac{\partial W_f}{\partial\left(\dfrac{\partial w}{\partial x}(x,t)\right)} \delta\left(\frac{\partial w(x,t)}{\partial x}\right) + \frac{\partial W_f}{\partial\left(\dfrac{\partial^2 w(x,t)}{\partial x^2}\right)} \delta\left(\frac{\partial^2 w(x,t)}{\partial x^2}\right)}^{\text{Virtual energy gained due to fluid and virtual work due to base excitation}} + \overbrace{\frac{\partial W_f}{\partial v_{11}(t)} \delta v_{11}(t) + \frac{\partial W_f}{\partial v_{12}(t)} \delta v_{12}(t)}^{\text{Virtual work based on generalised voltages}} \ . \tag{28.2}$$

Using the variational operations, the weak form-based Ritz method [74,75] can be further developed to formulate the solution requiring a test function which is a piecewise continuous function over the entire domain of the coupled system. The function must meet continuity requirements and the boundary conditions of the system. After manipulation and simplification, the reduced Eq. (12) can be formulated using Eqs. (17), (20), (22), (23) and (26) in terms of Eqs. (28.1)-(28.2) to give,

$$\int_{t_1}^{t_2}\left[\int_0^L \sum_{n=1}^{2} H_n(x)\left\{\left(I_{2n}+I_2^f\right)\frac{\partial \dot{w}(x,t)}{\partial x}\frac{\partial \delta w(x,t)}{\partial x}+\left(\left(I_{0n}+M^f\right)\ddot{w}(x,t)+\left(I_{0n}+M^f\right)\ddot{w}_{base}(t)\right)\delta w(x,t)\right.\right.$$

$$+2I_2^f U\frac{\partial^2 \dot{w}(x,t)}{\partial x^2}\frac{\partial \delta w(x,t)}{\partial x}+2M^f U\frac{\partial \dot{w}(x,t)}{\partial x}\delta w(x,t)+I_2^f U^2\frac{\partial^3 w(x,t)}{\partial x^3}\frac{\partial \delta w(x,t)}{\partial x}$$

$$\left.+M^f U^2\frac{\partial^2 w(x,t)}{\partial x^2}\delta w(x,t)+C_{tn}\frac{\partial^2 w(x,t)}{\partial x^2}\frac{\partial^2 \delta w(x,t)}{\partial x^2}\right\}\mathrm{d}x-\int_0^L\left(\sigma_1 v_{11}(t)+\sigma_2 v_{12}(t)\right)H_1(x)\frac{\partial^2 \delta w(x,t)}{\partial x^2}\mathrm{d}x$$

$$+H_2(x)\left\{x_c I_0^{tip}\frac{\partial \ddot{w}(L_2,t)}{\partial x}+I_0^{tip}\ddot{w}(L_2,t)+I_0^{tip}\ddot{w}_{base}(t)\right\}\delta w(L_2,t)$$

$$+H_2(x)\left\{I_2^{tip}\frac{\partial \ddot{w}(L_2,t)}{\partial x}+x_c I_0^{tip}\ddot{w}(L_2,t)+x_c I_0^{(tip)}\ddot{w}_{base}(t)\right\}\delta\frac{\partial w(L_2,t)}{\partial x}$$

$$\left.-\left\{\int_0^L \sigma_1 H_1(x)\frac{\partial^2 w(x,t)}{\partial x^2}\mathrm{d}x+C_{v1}v_{11}(t)\right\}\delta v_{11}(t)-\left\{\int_0^L \sigma_2 H_1(x)\frac{\partial^2 w(x,t)}{\partial x^2}\mathrm{d}x+C_{v2}v_{12}(t)\right\}\delta v_{12}(t)-q_{11}(t)\delta v_{11}(t)-q_{12}(t)\delta v_{12}(t)\right]\mathrm{d}t=0\,. \quad (29)$$

Note that since the pipe structure conveying fluid has the two segmented smart material components on the layer of the circumference region at the polar coordinate system, some coefficients can be seen in Appendix A, B and C where the coefficients of proof mass offset I_0^{tip} and I_2^{tip} are similar to those given by Lumentut and Friswell [34]. The voltage equation including its derivative, can be formulated using KVL for the internal piezoelectric connection in Fig. 1, giving,

$$v_1 = v_{11}+v_{12}\,,\ q_1 = q_{11} = q_{12}\ , \quad (30.1)$$

$$\dot{v}_1 = \dot{v}_{11}+\dot{v}_{12}\,,\ \ i_1 = i_{11} = i_{12}\ . \quad (30.2)$$

The harvesting circuit in Fig. 1 can also be formulated using KCL as,

$$i_1 = i_2 + i_3\ . \quad (31)$$

For the harvesting circuit using (31), the parallel R_dC_d circuit can be solved to give,

$$i_1 = C_d\dot{v}(t)+\frac{v(t)}{R_d}\,. \quad (32)$$

The solution in the normalised eigenfunction series form can be formulated as,

$$w(x,t) = \sum_{r=1}^{n}\hat{W}_r(x)w_r(t)\quad . \quad (33)$$

As shown in Eqs. (30.1) and (33), compact system equations reduced from Eq. (29) by including the mechanical damping coefficients were obtained after simplification,

$$\underbrace{M_{qr}^m\ddot{w}_r+C_{qr}^m\dot{w}_r+K_{qr}^m w_r}_{\text{Mechanical System}}+\overbrace{\Gamma_{q1}v_{11}+\Gamma_{q2}v_{12}}^{\text{Electromechanical Systems 1 \& 2}}=-\overbrace{\left(M_{qr}^f\ddot{w}_r+C_{qr}^f\dot{w}_r+K_{qr}^f w_r\right)}^{\text{Hydro-Elastodynamic System}}-\overbrace{\left(Q_q^f+Q_q^m\right)\ddot{w}_{base}(t)}^{\text{Base Excitation due to Fluid and Structure}}, \quad (34.1)$$

$$\overbrace{\Gamma_{r1}\dot{w}_r-C_{v1}\dot{v}_{11}(t)=i_{11}(t)}^{\text{Electromechanical System 1}}\ ,\quad \overbrace{\Gamma_{r2}\dot{w}_r-C_{v2}\dot{v}_{12}(t)=i_{12}(t)}^{\text{Electromechanical System 2}}. \quad (34.2)$$

Corresponding to Eqs. (30.2) and (32), Eq. (34.2) becomes,

$$\left(\frac{\Gamma_{r1}}{C_{v1}}+\frac{\Gamma_{r2}}{C_{v2}}\right)\dot{w}_r-\left(C_d\dot{v}(t)+\frac{v(t)}{R_d}\right)\left(\frac{1}{C_{v1}}+\frac{1}{C_{v2}}\right)-\dot{v}(t)=0\,. \quad (34.3)$$

where,

$$M_{qr}^{m}=\int_0^L\sum_{n=1}^{2}H_n(x)\left(I_{2n}\frac{\mathrm{d}\hat{W}_q(x)}{\mathrm{d}x}\frac{\mathrm{d}\hat{W}_r(x)}{\mathrm{d}x}+I_{0n}\hat{W}_q(x)\hat{W}_r(x)\right)\mathrm{d}x+I_0^{tip}H_2(x)\hat{W}_q(L_2)\hat{W}_r(L_2)\ ,\tag{34.4}$$

$$+H_2(x)\left(x_cI_0^{tip}\hat{W}_q(L_2)\frac{d\hat{W}_r(L_2)}{dx}+x_cI_0^{tip}\frac{\mathrm{d}\hat{W}_q(L_2)}{\mathrm{d}x}\hat{W}_r(L_2)+I_2^{tip}\frac{\mathrm{d}\hat{W}_q(L_2)}{\mathrm{d}x}\frac{\mathrm{d}\hat{W}_r(L_2)}{\mathrm{d}x}\right),\tag{34.5}$$

$$M_{qr}^{f}=\int_0^L\sum_{n=1}^{2}H_n(x)\left(M^f\hat{W}_q(x)\hat{W}_r(x)+I_2^f\frac{\mathrm{d}\hat{W}_q(x)}{\mathrm{d}x}\frac{\mathrm{d}\hat{W}_r(x)}{\mathrm{d}x}\right)\mathrm{d}x,\tag{34.6}$$

$$C_{qr}^{m}=c_vM_{qr}^{m}+c_dK_{qr}^{m}\ ,\tag{34.7}$$

$$C_{qr}^{f}=\int_0^L\sum_{n=1}^{2}H_n(x)\left(2M^fU\hat{W}_q(x)\frac{\mathrm{d}\hat{W}_r(x)}{\mathrm{d}x}+2I_2^fU\frac{\mathrm{d}\hat{W}_q(x)}{\mathrm{d}x}\frac{\mathrm{d}^2\hat{W}_r(x)}{\mathrm{d}x^2}\right)\mathrm{d}x\quad ,\tag{34.8}$$

$$K_{qr}^{m}=\int_0^L\sum_{n=1}^{2}C_{tn}H_n(x)\frac{\mathrm{d}^2\hat{W}_q(x)}{\mathrm{d}x^2}\frac{\mathrm{d}^2\hat{W}_r(x)}{\mathrm{d}x^2}\mathrm{d}x,\tag{34.9}$$

$$K_{qr}^{f}=\int_0^L\sum_{n=1}^{2}H_n(x)\left(M^fU^2\hat{W}_q(x)\frac{\mathrm{d}^2\hat{W}_r(x)}{\mathrm{d}x^2}+I_2^fU^2\frac{\mathrm{d}\hat{W}_q(x)}{\mathrm{d}x}\frac{\mathrm{d}^3\hat{W}_r(x)}{\mathrm{d}x^3}\right)\mathrm{d}x,\tag{34.10}$$

$$\Gamma_{r1}=-\int_0^L\sigma_1H_1(x)\frac{\mathrm{d}^2\hat{W}_r(x)}{\mathrm{d}x^2}\mathrm{d}x\ ,\qquad \Gamma_{r2}=-\int_0^L\sigma_2H_1(x)\frac{\mathrm{d}^2\hat{W}_r(x)}{\mathrm{d}x^2}\mathrm{d}x\ ,\tag{34.11}$$

$$\Gamma_{q1}=-\int_0^L\sigma_1H_1(x)\frac{\mathrm{d}^2\hat{W}_q(x)}{\mathrm{d}x^2}\mathrm{d}x\ ,\qquad \Gamma_{q2}=-\int_0^L\sigma_2H_1(x)\frac{\mathrm{d}^2\hat{W}_q(x)}{\mathrm{d}x^2}\mathrm{d}x\ ,\tag{34.12}$$

$$D_p=\frac{1}{C_{v1}}+\frac{1}{C_{v2}},\tag{34.13}$$

$$Q_q^f=\int_0^L\sum_{n=1}^{2}M^fH_n(x)\hat{W}_q(x)\mathrm{d}x\ ,\ Q_q^m=\int_0^L\sum_{n=1}^{2}I_0H_n(x)\hat{W}_q(x)\mathrm{d}x+H_2(x)\left(I_0^{tip}\hat{W}_q(L_2)+x_cI_0^{tip}\frac{\mathrm{d}\hat{W}_q(L_2)}{\mathrm{d}x}\right).\tag{34.14}$$

It is clearly seen that Eqs. (34.1) and (34.3) are different to those given in [34] and these be compared in the next section.

2.3. Modified equations of motion and frequency response equations

In relation to the flow profile modification factors for the laminar flow and turbulent flow implied in Eqs. (3.1)-(3.4) and (10.1)-(10.4), the flow profile is non-uniform and the fluid parameters from Eqs. (34.8) and (34.10) can be updated conveniently where they become $\overline{C}_{qr}^{f}=\beta_1^p\overline{C}_{qr}^{f1}+\beta_2^p\overline{C}_{qr}^{f2}$ and $\overline{K}_{qr}^{f}=\alpha_1^p\overline{K}_{qr}^{f1}+\alpha_2^p\overline{K}_{qr}^{f2}\ \forall p\in\{lam,turb\}$. The first and second parts of Eq. (34.8) can be reformulated to give $\overline{C}_{qr}^{f1}=\int_0^L\sum_{n=1}^{2}H_n(x)2M^f\overline{U}\hat{W}_q(x)\frac{\mathrm{d}\hat{W}_r(x)}{\mathrm{d}x}\mathrm{d}x$ and $\overline{C}_{qr}^{f2}=\int_0^L\sum_{n=1}^{2}H_n(x)2I_2^f\overline{U}\frac{\mathrm{d}\hat{W}_q(x)}{\mathrm{d}x}\frac{\mathrm{d}^2\hat{W}_r(x)}{\mathrm{d}x^2}\mathrm{d}x$, respectively. Similarly, the first and second parts of Eq. (34.10) can also be reformulated to give $\overline{K}_{qr}^{f1}=\int_0^L\sum_{n=1}^{2}H_n(x)M^f\overline{U}^2\hat{W}_q(x)\frac{\mathrm{d}^2\hat{W}_r(x)}{\mathrm{d}x^2}\mathrm{d}x$ and $\overline{K}_{qr}^{f2}=\int_0^L\sum_{n=1}^{2}H_n(x)I_2^f\overline{U}^2\frac{\mathrm{d}\hat{W}_q(x)}{\mathrm{d}x}\frac{\mathrm{d}^3\hat{W}_r(x)}{\mathrm{d}x^3}\mathrm{d}x$, respectively.

By considering the smart pipe conveying fluid under the Euler-Bernoulli beam assumptions, the second mass moment of inertias of the pipe structure and the fluid (I_2 and I_2^f) can be ignored. But, all mass moment of inertias of the proof mass offset should be included. Also, the fluid gravity effects and pressurisation were neglected at the beginning of the derivations for simplicity due to the relative meso-scale pipe system. With existence of non-uniform flow profile, Eqs. (34.1) and (34.3) must be modified by applying normalisation with the index notation as,

$$\left(\delta_{qr}+\hat{M}_{qr}^{f}\right)\ddot{w}_r(t)+\left(2\delta_{qr}\zeta_r\omega_r+\hat{C}_{qr}^{f}\right)\dot{w}_r(t)+\left(\delta_{qr}\omega_r^{2}+\hat{K}_{qr}^{f}\right)w_r(t)+\Gamma_{q1}v_{11}+\Gamma_{q2}v_{12}=-\left(Q_q^{f}+Q_q^{m}\right)\ddot{w}_{base}(t), \qquad (35)$$

Eq. (35) reflects the modified formulation due to the existence of flow-profile modification factors, and these factors have a direct relationship with the Reynolds number and Darcy friction factor. The updated fluid parameters from Eq. (35) can be reduced to give,

$$\hat{M}_{qr}^{f}=\int_0^L\sum_{n=1}^{2}M^{f}H_n(x)\hat{W}_q(x)\hat{W}_r(x)\,\mathrm{d}x\,,\quad \hat{K}_{qr}^{f}=\alpha_1^{p}K_{qr}^{f1}=\int_0^L\sum_{n=1}^{2}\alpha_1^{p}M^{f}\bar{U}^{2}H_n(x)\hat{W}_q(x)\frac{\mathrm{d}^2\hat{W}_r(x)}{\mathrm{d}x^2}\,\mathrm{d}x\,, \qquad (36.1)$$

$$\hat{C}_{qr}^{f}=\beta_1^{p}C_{qr}^{f1}=\int_0^L\sum_{n=1}^{2}2\beta_1^{p}M^{f}\bar{U}H_n(x)\hat{W}_q(x)\frac{\mathrm{d}\hat{W}_r(x)}{\mathrm{d}x}\,\mathrm{d}x\,. \qquad (36.2)$$

By applying Laplace transformations to Eqs. (34.3) and (35), the transfer functions of the multi-mode electromechanical coupled equations of motion are,

$$\left(\left(\delta_{qr}+\hat{M}_{qr}^{f}\right)s^2+\left(2\delta_{qr}\zeta_r\omega_r+\hat{C}_{qr}^{f}\right)s+\delta_{qr}\omega_r^{2}+\hat{K}_{qr}^{f}+\frac{\Gamma_{q1}\Gamma_{r1}}{C_{v1}}+\frac{\Gamma_{q2}\Gamma_{r2}}{C_{v2}}\right)W(s)$$

$$-\frac{s}{\left(\frac{1}{C_{v1}}+\frac{1}{C_{v2}}\right)}\left(\frac{\Gamma_{q1}}{sC_{v1}}+\frac{\Gamma_{q2}}{sC_{v2}}\right)V(s)=-\left(Q_q^{f}+Q_q^{m}\right)s^2W_{base}(s)\,, \qquad (37.1)$$

$$s\left(\frac{\Gamma_{r1}}{C_{v1}}+\frac{\Gamma_{r2}}{C_{v2}}\right)W(s)-\left(\left(sC_d+\frac{1}{R_d}\right)\left(\frac{1}{C_{v1}}+\frac{1}{C_{v2}}\right)+s\right)V(s)=0\,. \qquad (37.2)$$

After simplification, the electric voltage frequency response functions (FRFs) related to the non-uniform flow and the mechanical and electromechanical systems can be formulated in terms of the index notation as,

$$\frac{v(j\omega)}{-\omega^2 w_{base}e^{j\omega t}}=\frac{D_p\underset{(1\times n)}{\Gamma_{rv}}\underset{(n\times n)}{\Psi}\left(\underset{(n\times 1)}{Q_q^{f}}+\underset{(n\times 1)}{Q_q^{m}}\right)}{-\underset{(1\times 1)}{D_p}-\underset{(1\times 1)}{\frac{D_p{}^2C}{j\omega}}+\underset{(1\times n)}{\Gamma_{rv}}\underset{(n\times n)}{\Psi}\underset{(n\times 1)}{\Gamma_{qv}}}, \qquad (38.1)$$

where

$$\underset{(1\times 1)}{C=\left(j\omega C_d+\frac{1}{R_d}\right)},\ \underset{(1\times 1)}{D_p=\left(\frac{1}{C_{v1}}+\frac{1}{C_{v2}}\right)},\ \underset{(1\times n)}{\Gamma_{rv}=\left(\frac{\Gamma_{r1}}{C_{v1}}+\frac{\Gamma_{r2}}{C_{v2}}\right)},\ \underset{(n\times 1)}{\Gamma_{qv}=\left(\frac{\Gamma_{q1}}{C_{v1}}+\frac{\Gamma_{q2}}{C_{v2}}\right)}, \qquad (38.2)$$

$$\Psi=\left[-\omega^2\left(\underset{(n\times n)}{\delta_{qr}}+\underset{(n\times n)}{\hat{M}_{qr}^{f}}\right)+j\omega\left(\underset{(n\times n)}{2\delta_{qr}\zeta_r\omega_r}+\underset{(n\times n)}{\hat{C}_{qr}^{f}}\right)+\underset{(n\times n)}{\delta_{qr}\omega_r^{2}}+\underset{(n\times n)}{\hat{K}_{qr}^{f}}+\frac{\underset{(n\times 1)}{\Gamma_{q1}}\underset{(1\times n)}{\Gamma_{r1}}}{C_{v1}}+\frac{\underset{(n\times 1)}{\Gamma_{q2}}\underset{(1\times n)}{\Gamma_{r2}}}{C_{v2}}\right]^{-1}. \qquad (38.3)$$

The parameter n represents the number of normalised modes or degrees of freedom. The multi-mode electric current FRFs across the load resistance can be formulated as,

$$\frac{i_3(j\omega)}{-\omega^2 w_{base} e^{j\omega t}} = \frac{1}{R_d} \frac{v(j\omega)}{-\omega^2 w_{base} e^{j\omega t}} . \tag{39}$$

The power FRFs across the resistor and capacitor can be formulated, respectively, as,

$$\frac{P_{Cap}(j\omega)}{\left(-\omega^2 w_{base} e^{j\omega t}\right)^2} = j\omega C_d \left(\frac{v(j\omega)}{-\omega^2 w_{base} e^{j\omega t}}\right)^2 , \quad \frac{P_{\mathrm{Re}\,s}(j\omega)}{\left(-\omega^2 w_{base} e^{j\omega t}\right)^2} = \frac{1}{R_d} \left(\frac{v(j\omega)}{-\omega^2 w_{base} e^{j\omega t}}\right)^2 . \tag{40}$$

The optimal load resistance can be further formulated using the second part of Eq. (40) as,

$$R_d^{opt} = \left| \frac{jD_p}{\omega\left(-C_d D_p - 1 + \frac{1}{D_p} \Gamma_{rv} \Psi \Gamma_{qv}\right)} \right| . \tag{41}$$

Eq. (41) can be substituted into second part of Eq. (40) to give the optimal power output. The characteristic flow-induced electromechanical dynamic equation with n degrees-of-freedom in terms of the index notation can be formulated as,

$$\det \begin{bmatrix} \underset{(n\times n)}{\Psi}^{-1} & -\dfrac{\underset{(n\times 1)}{\Gamma_{qv}}}{D_p} \\ \underset{(1\times n)}{\Gamma_{rv}}\, j\omega & -\left(\underset{(1\times 1)}{\left(j\omega C_d + \dfrac{1}{R_d}\right)} \underset{(1\times 1)}{D_p} + 1 \right) \end{bmatrix} = 0 . \tag{42}$$

In Eq. (42), the complex polynomial roots of driving frequency ω based on the increasing flow velocity $\bar{U}$ can be determined using the Routh-Hurwitz stability criterion.

2.4 Electric output time history from AC-DC interface circuit

The segment of smart material layer from elastic pipe that generates the AC electric signal can be converted into a DC signal and further smoothed using a full-bridge rectifier and RC circuit. Fig. 3 shows the characteristic time history of the AC and DC voltages and currents during the process of pipe oscillation to convert the mechanical energy into an electrical signal. Therefore, the electrical signal output occurs when the excitation from the fluid flow is applied to the smart pipe. This implies that the reduced equations are still affected by the coupled system of the fluid, solid, circuit, and electromechanical components. Here, the following two electric cycle processes with the associated equations will be further solved using numerical methods.

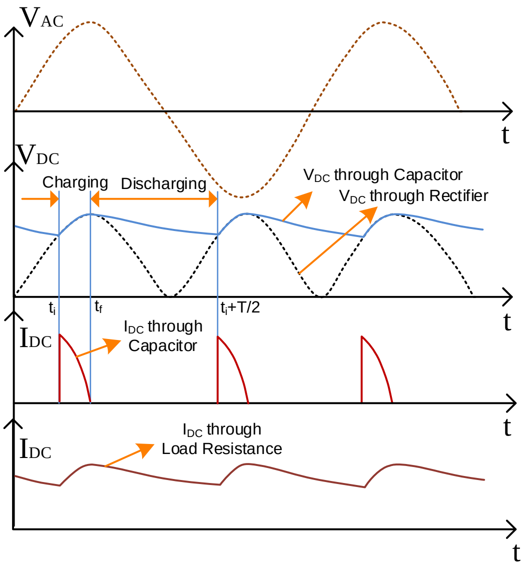

Fig.3 Time history of the standard harvesting circuit

a. Electric current in the interval $t_i < t < t_f$ indicating the charging time period for every half-cycle of the frequency.

The state space representation of the multi-mode response system can be formulated in terms of Eqs. (32), (34.3) and (35) to give,

$$\frac{\mathrm{d}}{\mathrm{d}t}\begin{Bmatrix} w_r(t) \\ \dot{w}_r(t) \\ v_d \end{Bmatrix} = \begin{bmatrix} a_{11} & a_{12} & a_{13} \\ a_{21} & a_{22} & a_{23} \\ a_{31} & a_{32} & a_{33} \end{bmatrix}\begin{Bmatrix} w_r(t) \\ \dot{w}_r(t) \\ v_d \end{Bmatrix} + \begin{Bmatrix} b_1 \\ b_2 \\ b_3 \end{Bmatrix}, \tag{43.1}$$

where: $a_{11} = a_{13} = a_{31} = 0$, $a_{12} = \delta_{qr}$, $b_1 = b_3 = 0$, (43.2)

$$b_2 = -\frac{\left(Q_q^f + Q_q^m\right)\ddot{w}_{base}(t)}{\left(\delta_{qr} + \hat{M}_{qr}^f\right)}, \quad a_{21} = -\frac{\left(\delta_{qr}\omega_r^{\ 2} + \hat{K}_{qr}^f\right)}{\left(\delta_{qr} + \hat{M}_{qr}^f\right)} - \frac{\dfrac{\Gamma_{q1}\Gamma_{r1}}{C_{v1}} + \dfrac{\Gamma_{q2}\Gamma_{r2}}{C_{v2}}}{\left(\delta_{qr} + \hat{M}_{qr}^f\right)}, \quad a_{22} = -\frac{\left(2\delta_{qr}\zeta_r\omega_r + \hat{C}_{qr}^f\right)}{\left(\delta_{qr} + \hat{M}_{qr}^f\right)}, \tag{43.3}$$

$$a_{23} = \frac{\left(\dfrac{\Gamma_{q1}}{C_{v1}} + \dfrac{\Gamma_{q2}}{C_{v2}}\right)}{D_p\left(\delta_{qr} + \hat{M}_{qr}^f\right)}, \quad a_{32} = \frac{\left(\dfrac{\Gamma_{r1}}{C_{v1}} + \dfrac{\Gamma_{r2}}{C_{v2}}\right)}{\left(C_d D_p + 1\right)}, \quad a_{33} = -\frac{D_p}{R_d\left(C_d D_p + 1\right)}. \tag{43.4}$$

b. Electric current with interval $t_f < t < t_i + T/2$ indicating the discharging time period for every half-cycle of the frequency.

The equation for the discharging period and its solution can be formulated, respectively as,

$$C_d\dot{v}_d + \frac{v_d}{R_d} = 0, \quad v_d(t) = v_d(t_f)\exp\left(\frac{-\left(t - t_f\right)}{C_d R_d}\right). \tag{44}$$

To plot the current and voltage time history signal during the charging and discharging periods, Eqs. (43.1) and (44) can be combined in the computational process. Note that the displacement and velocity time histories based on the flow velocity excitation can be computationally obtained using Eq. (43.1). As previously shown, the non-uniform flow velocity in steady conditions was formulated. However, pulsating flow in the pipe often occurs when the flow entering the inlet of the pipe is perturbed by a pump or valve or flow regulator. Here, the pulsating flow velocity with harmonic perturbations [27,28,32] can be assumed as,

$$\bar{U} = \bar{U}_o \left(1 + \lambda \cos \omega_v t\right) . \tag{45}$$

where ω_v is the flow pulsating frequency, $\bar{U}_o$ is the constant mean flow velocity, and λ is a small excitation parameter. Eq. (45) can simply be substituted into Eq. (43.1) in terms of Eqs. (36.1)-(36.2).

3 Results and discussion

This section provides two parametric studies. The first part discusses the phenomena of smart pipe dynamics due to the effects of the flow profile and base excitation. It elaborates detailed cases of hydro-electro-elastic stability and instability for generating the optimal power output. The second part discusses various comparisons of the physical parameters using the fluid flow effects either with or without the existence of base excitation to the smart pipes.

3.1. Interactions between flow dynamics and base excitation

This section focuses on discussions of the dynamic stability and instability of the smart pipe with an offset proof mass due to fluid flow. All of the data analyses use the weak form-based Ritz method analytical approach based on the four-term approximation. This analytical approximation was obtained from the exact solution of the cantilevered smart pipe and the equations are given by Lumentut and Friswell [34]. Initially, the current method in comparison with the Hamiltonian method with flow-charge coupling is discussed in terms of the root locus of the Argand diagram and the 3-D frequency response system based on the variable flow velocity. It is important to note here that this initial validation is based on the ideal flow profile in the smart pipe structure. However, further discussions based on the non-uniform flow profile in the smart pipe will be given, to show how the real flow system (the relationship between Darcy friction factor, Reynolds numbers, and flow profile modification factor) can directly induce the smart integrated physical system consisting of the solid (elastic piezoelectric pipe structure), circuit, and electromechanical components to produce the optimal electric power output. The flow system phenomena in the smart pipe based on the eigenfrequency locus, frequency response, absolute velocity time history, and dynamic evolution of the physical structure will be elaborated. The alternative smart material of the pipe structure using electroactive polymer material (EAP) film will also be discussed to analyse the potential to generate electrical power and for the flutter control application.

Table 1. Material properties

Material properties	Piezoelectric	Electroactive polymer	Silicon elastomer	Fluid
Young's modulus, $\bar{c}_{11}$ (GPa)	66	5	0.025	-
Density, ρ (kg/m^3)	7800	1500	1200	1000
Piezoelectric constant, d_{31} (pm/V)	-190	28.2	-	-
Permittivity, ε_{33}^T (F/m)	1800 ε_o	16 ε_o	-	-
Permittivity of free space, ε_o (pF/m)	8.854	8.854	-	-

Since there are two different physical properties, each smart pipe with different structural components consisting of the substructure and active layers can be found in Table 1. The first smart pipe was made of silicon elastomer and PZT PSI-5A4E, while the second smart pipe was made of silicon elastomer and EAP. The length (L) for both smart pipes was 150 mm. The geometry parameters for the first smart pipe with inner radius, substructure thickness, and PZT thickness were set to 6 mm, 1.6 mm, 0.1 mm, respectively. The load resistance R_d=100 kΩ and capacitance C_d = 0.1 μF were chosen for this study. The physical dimensions of the second smart pipe with inner radius, substructure thickness, and EAP thickness were set to 6 mm, 1.6 mm, 30 μm, respectively. Note that the EAP film is relatively thin and flexible with quite high elastic modulus. The dimensions of the proof mass offset, namely length l_t, and inner and outer radii (r_{t1} and r_{t2}), were set to 8 mm and 10 mm and 7.6 mm, respectively. The mass of fluid per unit length M^f was set to 0.11 kg/m. The input base acceleration was set to be 3 m/s^2. Again, all parameters are defined in Fig. 1. The segmented smart pipe structure (L_1 = 0.06 m and L_2 = 0.09 m) and the circumference electrode segments for the upper and lower regions ($\beta_1 - \alpha_1$ = 144∘ and $\beta_2 - \alpha_2$ = 144∘) were utilised for the analysis because the physical geometries can provide the optimal response [34].

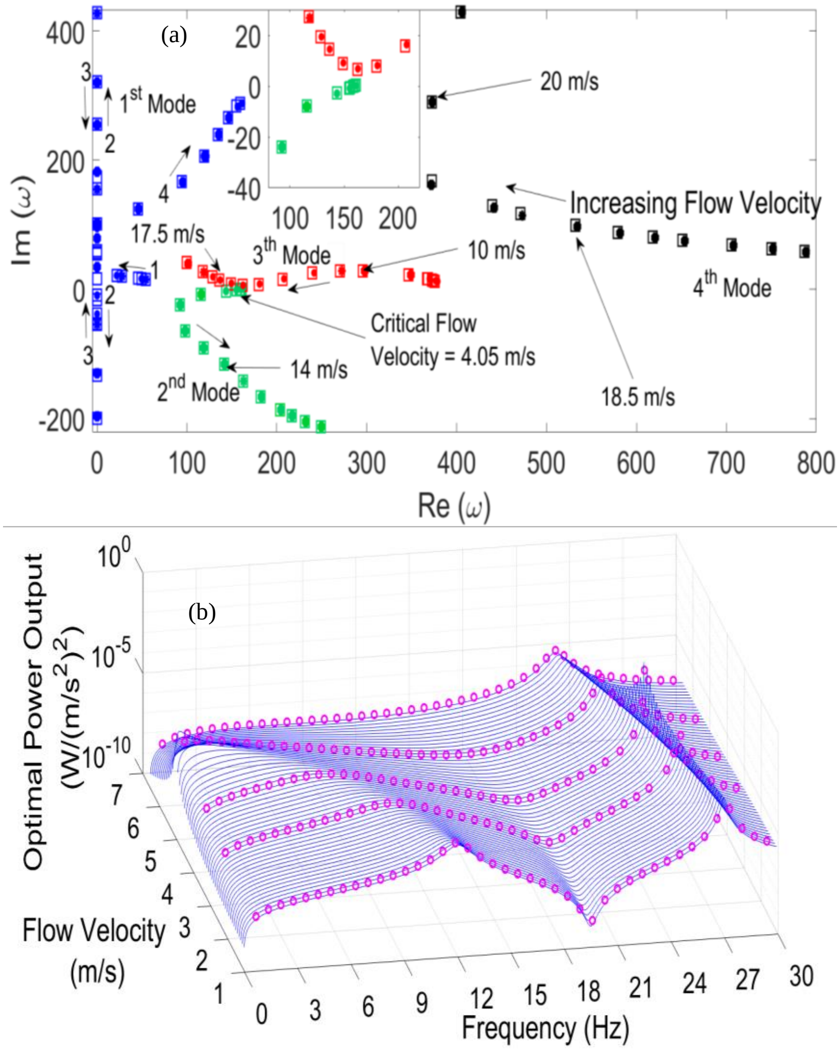

Fig. 4. System responses of the PZT pipe with uniform flow profile using the flow-voltage-type Hamiltonian method (dot-(a) & round-(b)) and the flow-charge-type Hamiltonian method (square-(a) & line-(b)): (a) Argand diagram and (b) 3-D optimal power output FRFs at the first and second modes.

In Fig.4, the trends in the Argand diagram and 3-D frequency responses under variable flow velocity using the two different methods show good agreement. The system responses of the smart pipe as shown here were calculated under a uniform flow profile or ideal flow. The results shown in Fig. 4 include the comparisons between the current method and Hamiltonian method with flow-charge coupling [34]. It is clearly seen that the stability at the second mode is initially gained by the smart pipe. However, the system becomes unstable by flutter beyond the critical flow velocity of 4.06 m/s. Note that the mode shown in the system response is affected by the physical interactions of the fluid, solid, circuit, and electromechanical systems. The first mode gains stability, although a divergent instability is also observed with increasing flow velocities but does not occur any longer because it returns to be stable with increasing further flow velocities. For the third mode, although the roots of the complex frequencies, corresponding with increasing flow velocities, are closer to the positive real axis, the roots do not coincide on that axis or approach a purely real value to show the onset of flutter. At this point, a stable response predominantly occurs with increasing flow velocities. The fourth mode clearly shows a stable response. In Fig. 4, the optimal power output FRFs under variable flow velocity is given for the frequency range spanning the first two modes. Again, the first mode gains stability with increasing flow velocity resulting in a reduction of the power amplitude with shifting resonance frequency. The second mode, however, shows an increase of optimal power output with increasing flow velocity until reaching its critical value. Then, the power output drops gradually above the critical flow velocity. Note that the selected data points (circle) represent the current method. Also note that the identification of the onset of instability as shown here provides an accurate dynamic instability response. The whole scenario of Fig. 4 obviously shows further proof and has similar response to that of the dynamic response from the Argand diagram.

Further technical aspects of the dynamic stability/instability behaviour under variable flow velocity with the non-uniform flow profile can be seen in Fig. 5. It is important to note here that since the data analyses using the results shown in Fig.5a-5e are related to each other, the discussion will be combined at this stage. Compared to the Argand diagram in Fig. 4a, the characteristic dynamic responses for the first four modes in Fig. 5a shows a similar phenomenon with slightly different values. This means that the contribution of flow profile modification factor into the coupled dynamic equations directly affect the eigenfrequency locii. Note that turbulent flow obviously occurs in this scenario. The flow profile modification factor depends on the Reynolds number and Darcy friction factor. For example, increasing the flow velocities or the Reynolds numbers, as shown in Fig. 5c, may result in decreasing the Darcy friction factor and the flow profile modification factor. Note that the turbulent log law appears when the Darcy friction factor and flow profile modification factor give the exponential decay (Fig. 5c). At certain value of the Darcy friction factor and the flow profile modification factor, the maximum optimal power output occurs at the level of turbulent flow (Fig. 5d) with the minimum optimal load resistance (Fig. 5e). Note that each Reynolds number associated with the flow profile modification factor has their own optimal power output and optimal load resistances in the frequency domain. Amongst those collective data points, certain optimal values can also give the maximum points of optimal power output associated with the minimum points of optimal load resistance (Fig. 5e & 5f). Here, the range of the flow profile modification factor has a small gap as it falls between 1.01 and 1.025 representing the range of turbulent flows (Figs. 5c & 5f). But, the effect of the non-ideal flow in the smart pipe produces the electrical energy based on the trend of dynamic stability and instability. With that range, the comparison between the ideal and non-ideal flow in a smart pipe gives a relatively small difference. Intuitively, the

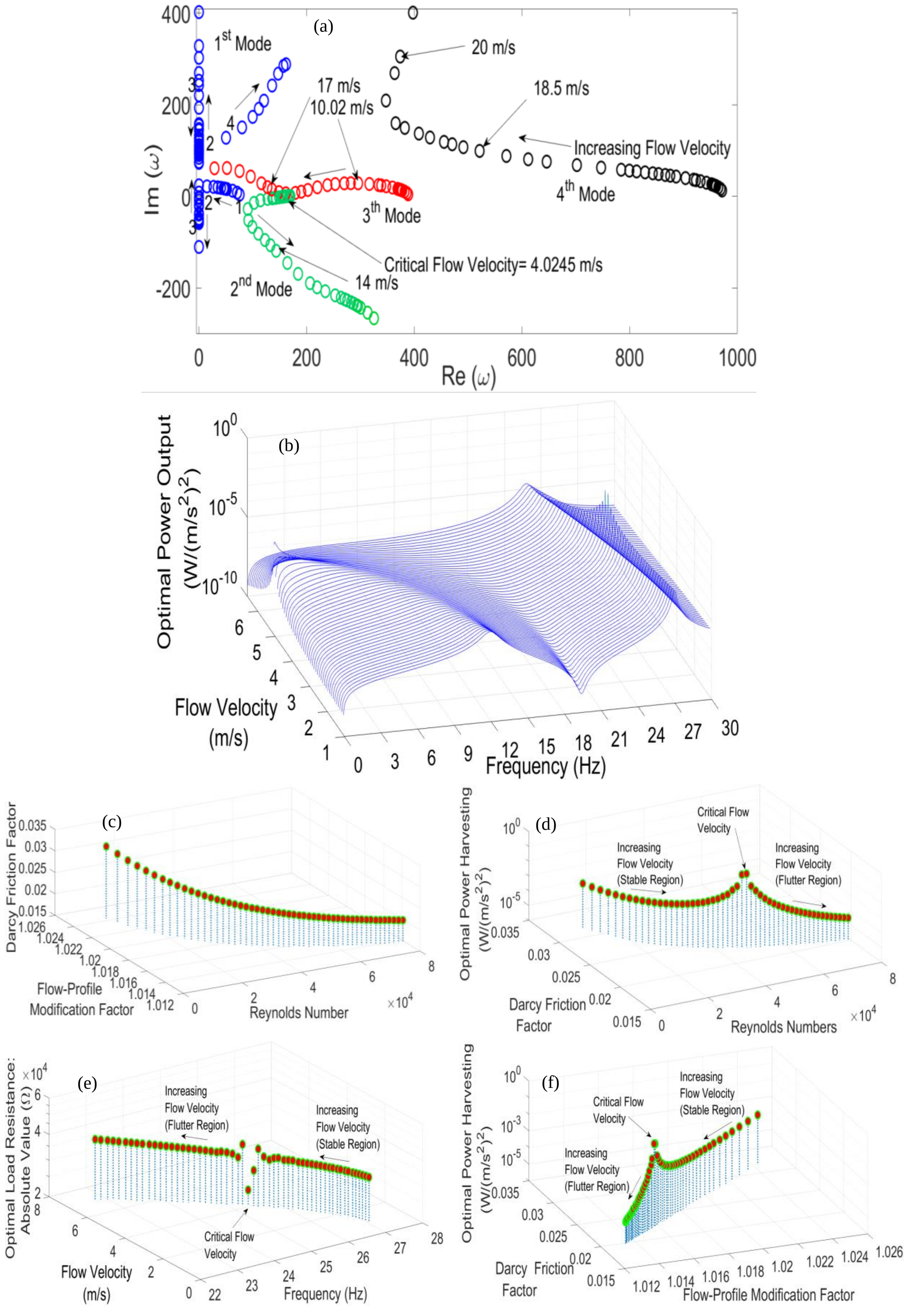

Fig. 5. System responses of the PZT pipe with the non-uniform flow profile: (a) Argand diagram, (b) 3-D optimal power output FRFs at the first and second modes, (c) relationship between flow profile modification factor, Reynolds number, and Darcy friction factor, (d) relationship between Darcy friction factor, Reynolds number, and optimal power output, (e) relationship between flow velocity, resonance frequency, and optimal load resistance, (f) relationship between Darcy friction factor, flow profile modification factor, and optimal power output.

difference can be a quite pronounced if the flow profile modification factor is set to be a higher value reaching 4/3 (1.333) for laminar flow. This scenario shows the same conclusion given by Guo et al. [66]. The case of the pipe conveying laminar flow in the energy harvesting application can be a challenging process in terms of proper geometry and design of the system in order to achieve the occurrence of the onset of flutter instability and lower critical flow velocity and the calculation of the maximum power output. The critical flow velocity at the second mode occurs at one locus point, giving 4.0245 m/s. Initially, a stable response is gained but does not occur any longer after reaching the first critical flow velocity of 4.0245 m/s. In Fig. 5b, the optimal power output FRFs with variable flow can give the peak or maximum point of resonance with the power output reaching 9.6 $mW/(m/s^2)^2$, representing the occurrence of the critical flow velocity. It is clearly seen that the frequency shift occurs when the flow velocity changes. In such situations, the power output at the second mode can also be achieved with decreasing resonance frequencies. Again, the non-uniform flow profile is still used for the analysis of smart pipe. In Fig. 5b, the optimal power output FRFs can be achieved at the first two modes. This phenomenon can obviously be proved where the Argand diagram (Fig. 5a) also shows the critical velocity at the second mode. Note that the next stage will discuss the effect of using the electroactive polymer material film for the smart pipe, which has a much lower onset of the flutter instability compared to the piezoelectric ceramic material.

Figure 6 shows the evolution of time history responses for three flow velocities. The absolute velocities at the tip end of the elastic pipe with variable frequency excitation show different patterns using the three different flow velocities. With constant flow velocity and variable frequency excitation, the stable response of the absolute velocity occurs, as shown in Fig. 6a. The peak of the absolute velocity occurs when the frequency of excitation is equal to the resonance frequency of 25.63 Hz. If the chosen frequency of excitation is quite away from the resonance of the system, the absolute velocities will tend to form different stable responses. The trend of the time history signals also shows the mixed beating signal pattern across off-resonances during the formation of stable signal response. When the frequency excitation is far away from the resonance region, the beat period becomes smaller. This series of events occurs because the time history of the structural smart pipe with the variable off-resonance tends to overlap with the fluid system at constant flow velocity. However, the trend shows predominantly stable responses over the frequency domain. For the beating time history phenomena shown in Fig. 6b, the fluid system response can be set using the critical flow velocity so as to coincide with the resonance frequency of the structural smart pipe. As a result, the majority of the absolute velocity time history across the range of frequency of excitation show a strong beat response. Furthermore, as shown in Fig. 6c, the flutter response of the absolute velocity time history occurs across off-resonances when the flow velocity is set to increase over its critical value. Although there is the mixed beating response over the time domain, the signal of the flutter instability provides a strong response because its natural phenomenon commonly gives the time history signal that grows continuously with oscillation and without bound. By viewing the dynamic evolution shown in Fig. 7, the physical model for the elastic smart pipe moves at any instant in time due to different flow velocities and increment of particular frequency of excitation. Note that the physical motion was taken as a snapshot of the absolute velocity time history over one period. The series of events of the system shows comprehensive spatial and temporal dynamic behaviour representing the effect of fluid flow within the integrated smart structure with the electromechanical system and the harvesting circuit. The dynamic evolution of the physical system becomes interesting and somehow shows unexpected shapes. In general, they immediately look like the second mode shape with zero fluid flow. Indeed, the results shown in Fig. 7 were obviously taken around the second mode with different fluid flow and frequency of excitation. Hence they naturally show similarity with the second mode shape with zero fluid flow. The reason why the second mode shape was considered here is because the critical flow velocity and the onset of flutter instability occur.

As shown previously with different case studies, turbulent flow can occur within the smart pipe. For certain turbulent flow, the peak power output at certain flow velocities across resonance frequency can be produced (Figs. 5d & 5f) where this situation is also used here for the dynamic evolution of the physical system. The effect of the frequency of excitation with constant geometry of the pipe is not implicitly and directly related to the Reynolds number calculation. It means that if the frequency excitation of the system changes, the Reynolds number will not change. But, the Darcy friction factor and Reynolds numbers implicitly and directly affect to the calculation of the flow-profile modification factor which is the main parameter for the centrifugal fluid force. In Fig. 7 shown here, the absolute velocities with different flow velocities and frequency excitations were taken near to the critical flow velocity of the system. The onset of the flutter instability, and slightly beyond it, with the turbulent flow at certain frequencies seems to be noticeable (Figs. 7h & 7k). The onset of flutter instability can be an essential identification for dynamic instability as proposed here. The future work of a nonlinear coupled system of the smart pipe due to the flutter instability with a Hopf bifurcation will be considered. Moreover, by scrutinising each segment of the smart pipe again, the first segment (L_1 = 0.06m) near the base support evolves different shapes while accumulating the absolute velocity values of this segment. The second segment (L_2 = 0.09m) tends to form a similar pattern but for different levels of oscillation. Note that the absolute velocity at the base support (L_1 = 0m) is not zero because the elastic smart pipe is also under base excitation due to the fluid and structure. Also note that the second segment is relatively more flexible than the first segment due to the stiffness parameter. But, the first segment can generate sufficiently high electrical power, even only giving a lower transverse absolute velocity of the smart pipe. This is because the cantilevered smart structural system obviously provides higher strain so as to induce the polarity of the piezoelectric component for generating electrical voltage. The first segment (L_1 = 0.06m) has two layers (PZT and silicon elastomer) and second segment (L_2 = 0.09m) has a single layer (silicon elastomer). For some cases, the first segment somehow looks like the third mode shape (Figs. 7h & k). At this point, when the absolute velocity at the base support at the negative points significantly moves to the positive points approaching the maximum level at instant times over one half-period, the end of the first segment response becomes negative and the second segment also continues to carry the negative points with large values. Conversely, another situation also occurs when the base support response becomes negative, the end of first segment continued with the second segment goes positive. However, by viewing a different trend (Figs. 7e & f), when the response of the base support shifts significantly positive, the end of the first segment followed by the second segment still goes positive. A similar trend also occurs in opposite direction. At some point for different dynamic evolution, when all of the moving base support (Fig. 7c & 7d) moves up at the positive axis, the end of the first segment, along with all of the second segment goes down and vice versa.

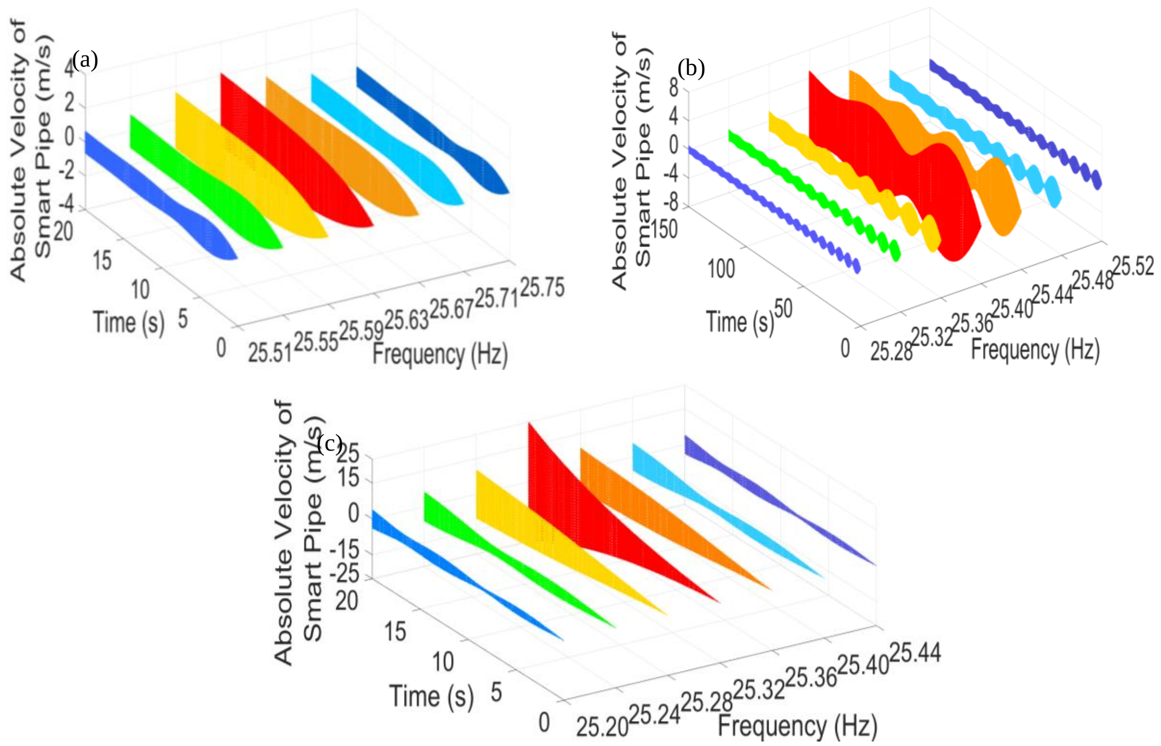

Fig. 6. Evolution of the absolute velocity-time waveform of the PZT pipe with the non-uniform flow profile under variable frequency excitation: (a) $\bar{U}$ =3.75 m/s, (b) $\bar{U}$ = 4.0245 m/s, and (c) $\bar{U}$ =4.15 m/s.

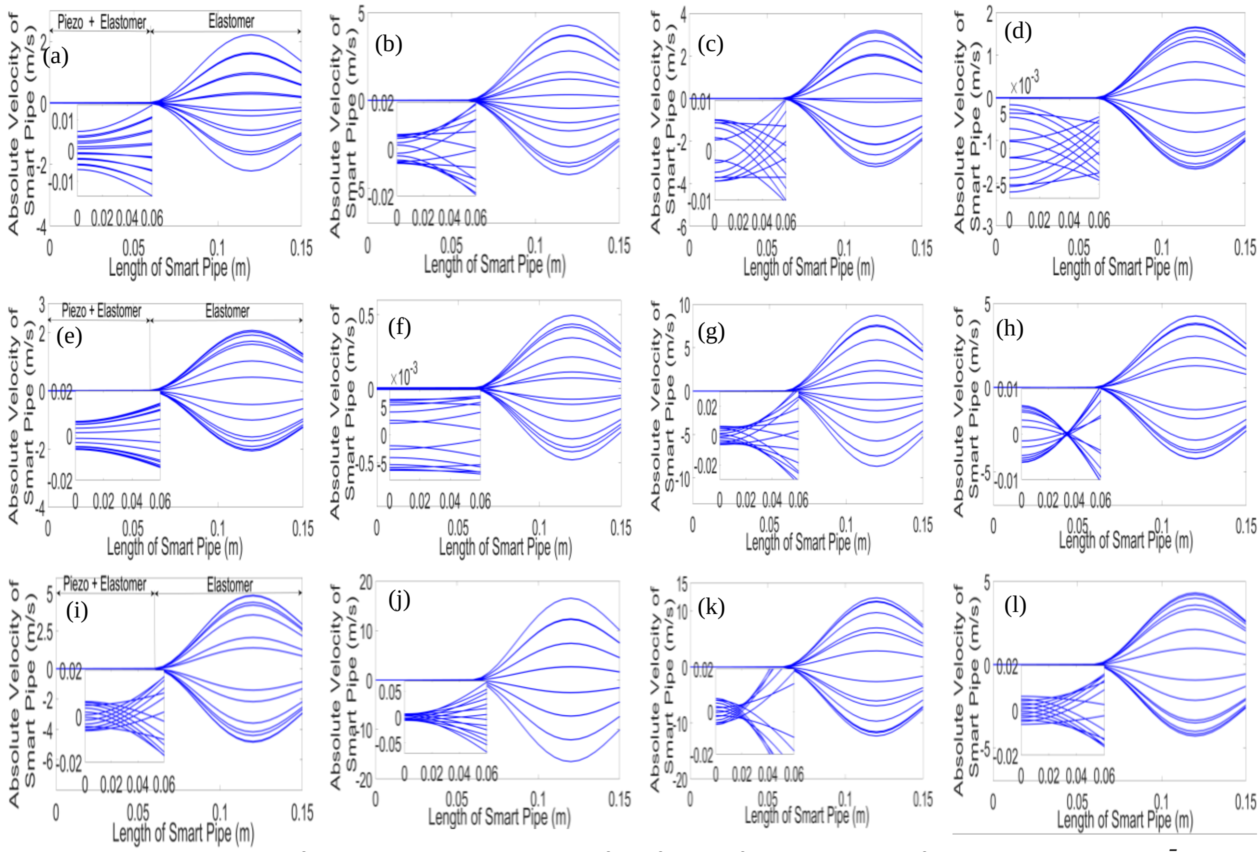

Fig. 7. Dynamic evolution of the PZT pipe with the non-uniform flow profile under variable frequency excitation: (a) $\bar{U}$ =3.75 m/s with 25.55 Hz, (b) $\bar{U}$ =3.75 m/s with 25.63 Hz, (c) $\bar{U}$=3.75 m/s with 25.67 Hz, (d) $\bar{U}$ =3.75 m/s with 25.71 Hz, (e) $\bar{U}$ =4.0245 m/s with 25.28 m/s, (f) $\bar{U}$ =4.0245 m/s with 25.32 Hz, (g) $\bar{U}$ = 4.0245 m/s with 25.44 Hz, (h) $\bar{U}$ = 4.0245 m/s with 25.48 Hz, (i) $\bar{U}$ =4.15 m/s with 25.24 Hz, (j) $\bar{U}$ =4.15 m/s with 25.32 Hz, (k) $\bar{U}$ =4.15 m/s with 25.36 Hz, (l) $\bar{U}$ =4.15 m/s with 25.40 Hz.

Discussion on the dynamic system responses using the electroactive polymer material (EAP) film embedded on the structural pipe under non-uniform flow profile are now presented to analyse the stability/instability behaviour, power output FRFs, and physical dynamic evolution. As shown in Fig. 8a, the prediction of the system dynamics for the smart pipe conveying fluid can be seen in the Argand diagram showing different characteristic responses as given in Fig. 5a. The second and third modes have two occurrences of onset of flutter instabilities with three different critical flow velocities corresponding with variable eigenfrequencies, whereas Fig. 5a only gave a single onset of flutter instability at the second mode. With the critical flow velocity of 2.568 m/s for the second mode, the onset of flutter instability appears earlier compared with the result shown in Fig. 5a. The repeated critical flow occurrence for the second mode with different critical flow velocities can be seen in Fig. 8a. The second mode initially gives a stable response. After reaching the first critical flow velocity of 2.568 m/s, the flutter instability is gained but does not occur any longer after reaching the second critical flow velocity of 13.0517 m/s. Beyond the second critical flow velocity, the stable response returns until reaching the higher flow velocity. A similar phenomenon also occurs for the optimal power output FRFs in Fig. 8b with the frequency shift and variable flow.

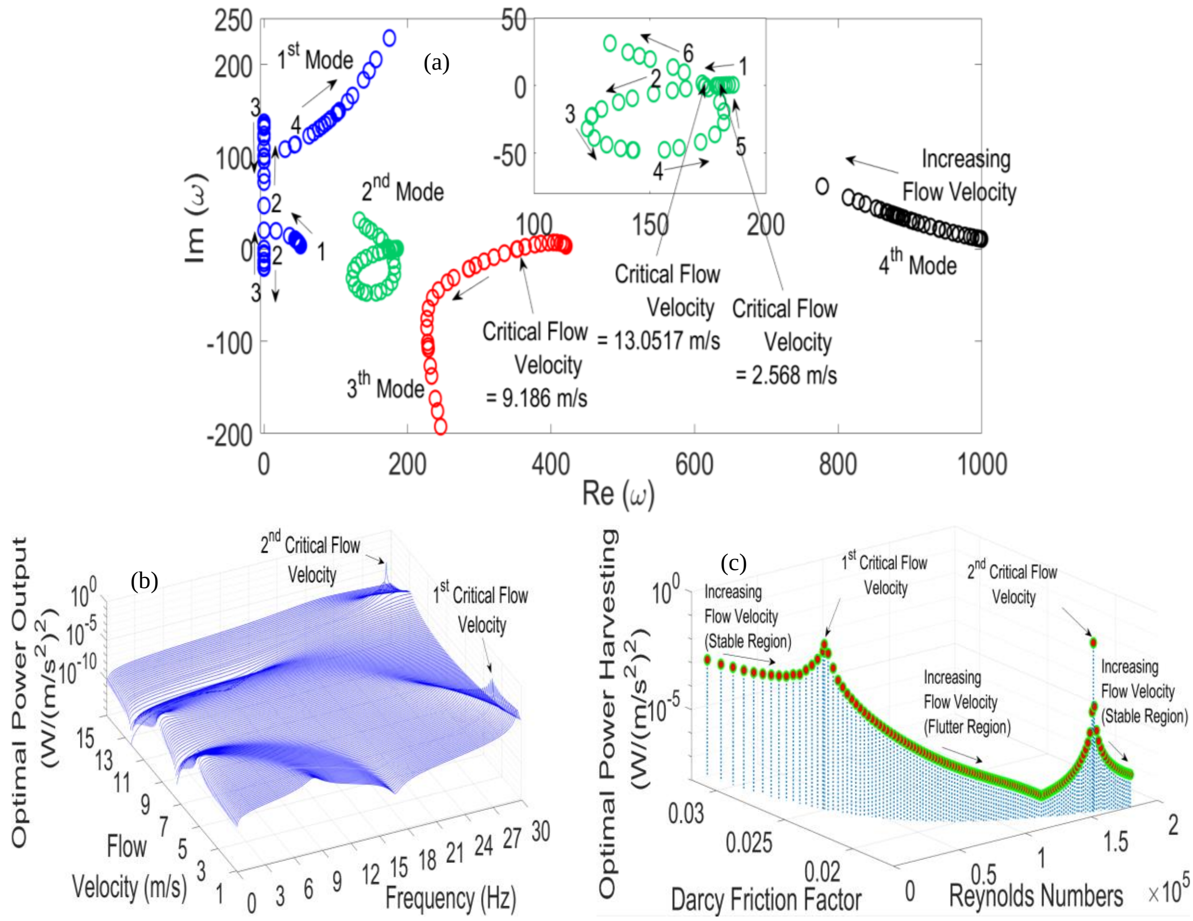

Fig. 8. System responses of the EAP pipe with the non-uniform flow profile: (a) Argand diagram, (b) 3-D optimal power output FRFs at the first and second modes, (c) relationship between Darcy friction factor, Reynolds number, and optimal power output at second mode.

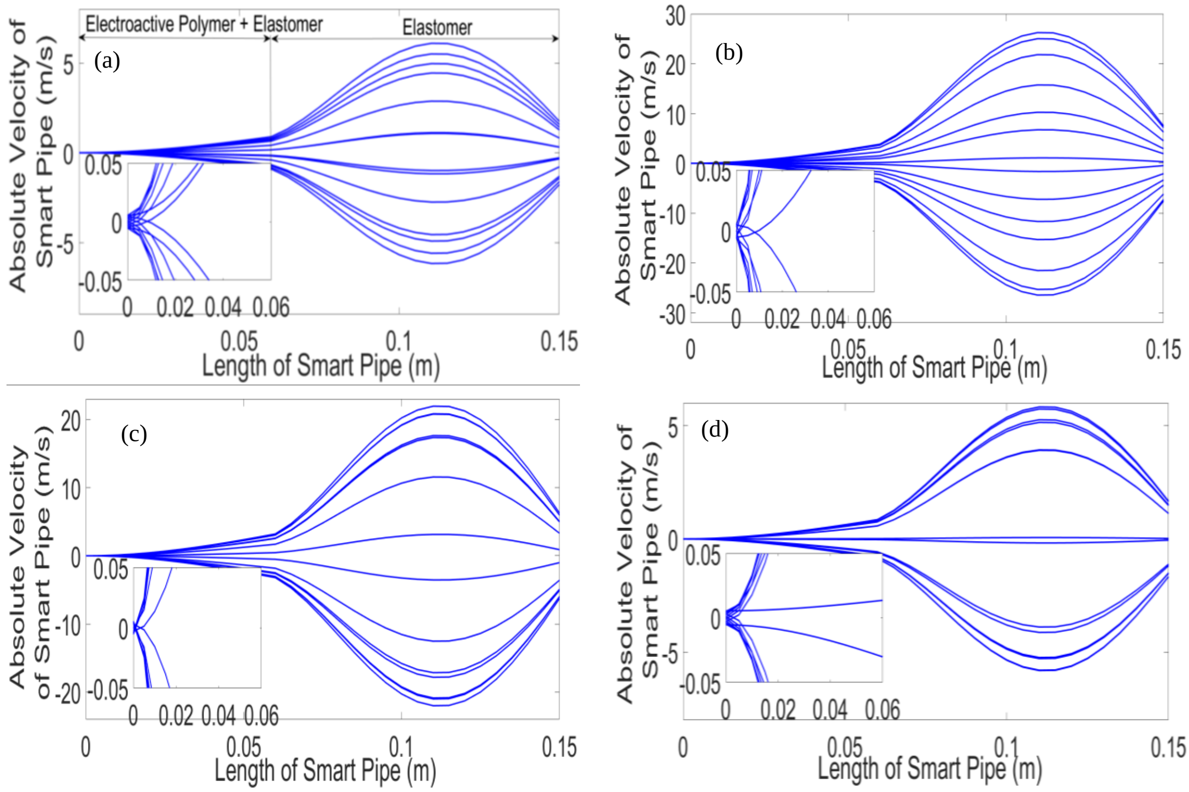

Fig. 9. Dynamic evolution of the EAP pipe with the non-uniform flow profile under variable frequency excitation: (a) $\bar{U}$ =2.76 m/s with 28.27 Hz, (b) $\bar{U}$ =2.76 m/s with 28.39 Hz, (c) $\bar{U}$=2.76 m/s with 28.43 Hz, (d) $\bar{U}$ =2.76 m/s with 28.51 Hz.

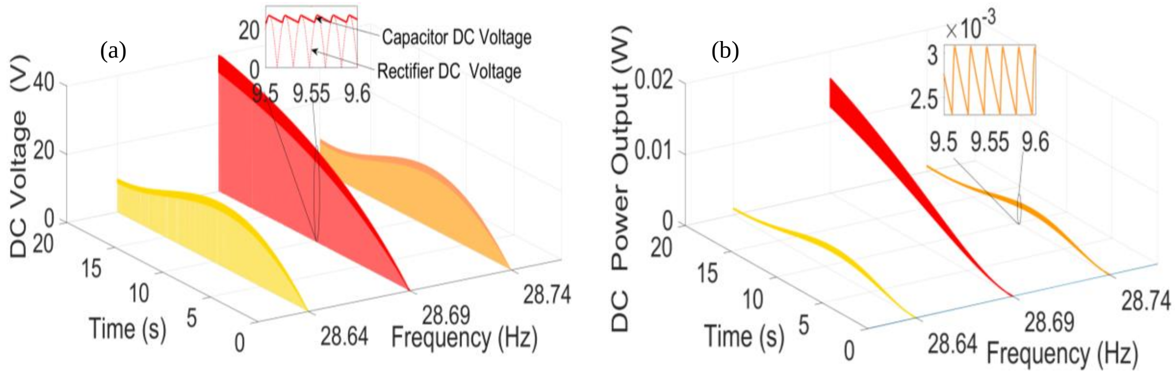

Fig.10. DC system responses of the EAP pipe with the non-uniform flow profile under frequency excitations: (a) voltage-time waveform across rectifier and capacitor, (b) power-time waveform across load resistance.

As shown, the two peaks of resonance with the occurrence of the onset of flutter instability provide power outputs reaching 101.5 mW/(m/s^2)^2 and 153.6 mW/(m/s^2)^2, respectively. This can also be seen in Fig. 8c where the two peaks of resonance of the power output can be achieved with different levels of Darcy friction factor and Reynolds number. This is relevant to the flutter control application for the smart pipe power harvester without needing higher flow velocity with stronger flutter. This can be used to avoid the fatigue of the structure itself over a long period of motion. Here, the smart pipe using the thin film material with fluid flow proves to be more effective due to lower velocities for the onset of the flutter instability compared to the smart pipe with the piezoelectric ceramic. This is because the flexibility of the thin film material, which has a relatively much lower modulus of elasticity compared with the piezoelectric ceramic material. The series of simulations for the physical system with flutter is chosen as examples here. Further proof can also be seen in Fig. 9 where the dynamic evolution of the thin film smart pipe shows different shapes to those shown in Fig. 7. In particular, the oscillations gradually grow along the first segment and continue to oscillate dramatically at different levels of absolute velocity. It is also clearly seen that the electroactive polymer pipe structure shows the flexibility of the first segment motion that evolves different shapes with wider oscillations.

For the DC time history response at different frequencies of excitation, the DC voltages across the full-bridge AC/DC rectifier and smoothing R_dC_d show different trends, as shown for example in Fig. 10. The process of capturing the AC/DC rectifier can be seen from the conversion of the AC signal from the smart pipe becoming the positive ripple signal due to the diode pairs (D1and D2) and (D3 and D4) interchangeably turning to conduct to give the DC signal. This ripple signal reduces due to the smoothing capacitor resulting in charging and discharging processes for every half-cycle. But, the DC voltage output depends on the chosen capacitor and resistor. The predictions of the AC and DC voltages including the power output across the load resistance before the onset of the flutter can be seen in the stable responses for the chosen frequencies of excitation at the resonance region. This can be seen that the voltage and power outputs at the middle of frequency excitation shows the maximum level. If the critical flow velocity is close, then the DC signal response will tend to form a flutter response.

3.2 Various comparisons between the physical parameters

In previous section, the dynamic phenomena of pipe structures under non-uniform flow profiles in a steady condition, coupled with the electromechanical system, have been examined. Here, the non-uniform flow in pipes, either with or without the existence of pulsation and base excitation, are further compared and examined. It is noted that the pulsating flow as a function of time-dependent harmonics is further superposed on a non-uniform flow in pipes, giving a complementary scientific perspective in a real application. The pipe structure energy harvesting is induced by the pulsating flow perturbed by a miniature jet flow valve so as to control the inlet flow to the pipe structure. Here, Eq. (45) was implemented where the flow pulsating frequency ω_v and small perturbation parameter λ were set to 8 Hz and 0.2, respectively. The physical dimensions and properties of silicon elastomer pipe structures with the embedded EAP material component and circuit parameters are set to have similar values to those used in the previous section. The numerical method was deployed by setting the initial static displacement conditions of pipe conveying fluid and fast Fourier transform (FFT) analysis was further used for the frequency spectrum analysis. As shown in Fig.11, the chosen flow velocities approaching the onset of flutter instability were taken for the dynamic analyses. Each flow velocity is used to examine the four different physical parameters. In a general context, the power outputs, starting with the highest amplitude, can be achieved from the non-uniform pulsating flow and with base excitation, followed by the non-uniform flow and with base excitation, the non-uniform pulsating flow and without base excitation, and the non-uniform flow and without base excitation. Also, the flow velocity of 2.568 m/s corresponding with the four physical parameters gives the highest amplitude of power output, followed by 2.540 m/s and 2.430 m/s. As shown, the second mode shape predominantly shows the maximum peak of resonance due to approaching the critical flow velocity and the onset of flutter instability. The appearance of spiking resonances in the frequency domain also occurs when the non-uniform pulsating flow in the pipe structure with and without base excitations are examined.

The evolution of time history responses for the three flow velocities shows the absolute velocities at the tip end of the elastic pipe. Stable responses given by a flow velocity of 2.430 m/s in Fig. 12a-d can be seen from the four physical parameters. However, the time history responses using the non-uniform flow & without base excitation and non-uniform pulsating flow & without base excitation appear to decay continuously. As the flow velocity is increased to 2.540 m/s, mixed time history signal behaviours occur using different physical parameters. Stable responses with continuous fluctuation and decay signals (Figs. 12e,f) can be seen in the non-uniform flow & with base excitation and non-uniform flow & without base excitation, respectively. For the stable responses, the pipe structure is clearly damped without base excitation where this is the most common phenomenon as shown in the previous literature. However, the inclusion of pulsating flow in the pipe even without base excitation may create an earlier flutter instability of the pipe structure (Fig. 12g). This is because the frequency excitation of flow pulsation may trigger a dynamic motion that is quite pronounced in the pipe structure. Note that the pipe itself has a characteristic mechanical dynamic behaviour (eigenfrequency). With the same flow velocity, the beating signal response occurs slightly for the non-uniform pulsating flow & with base excitation (Fig. 12h). Note that if the time domain is further expanded to more than 85 seconds, the signal will repeat its pattern to form the beating response. As compared to Fig. 12g, the inclusion of the base excitation may tune the dynamics of the pipe, having similar response to the fluid system. As shown in the previous section and discussed further here, the onset of the flutter instability occurs at a flow velocity of 2.568 m/s, as shown clearly in Fig. 12i. However, the signal patterns appear differently when considering other different physical parameters. For the non-uniform flow & without base excitation (Fig. 12j), stable responses with continuous fluctuation occurs. When the non-uniform pulsating flow & without base excitation is considered, the system becomes unstable by flutter (oscillation without bound). The stronger flutter response occurs when considering the non-uniform pulsating flow & with base excitation.

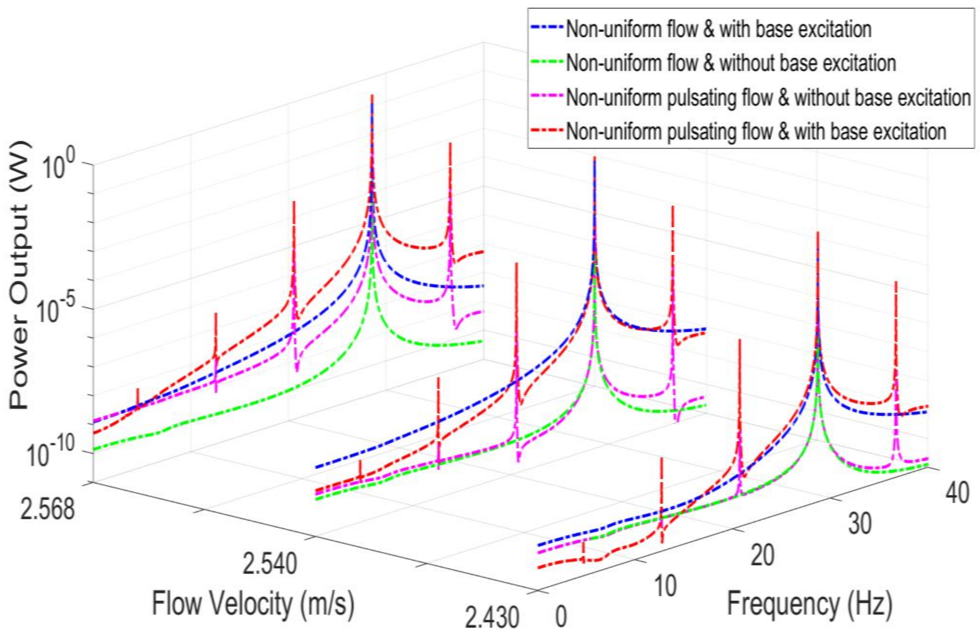

Fig.11. Power output FFT responses of the EAP pipe using different physical parameters.

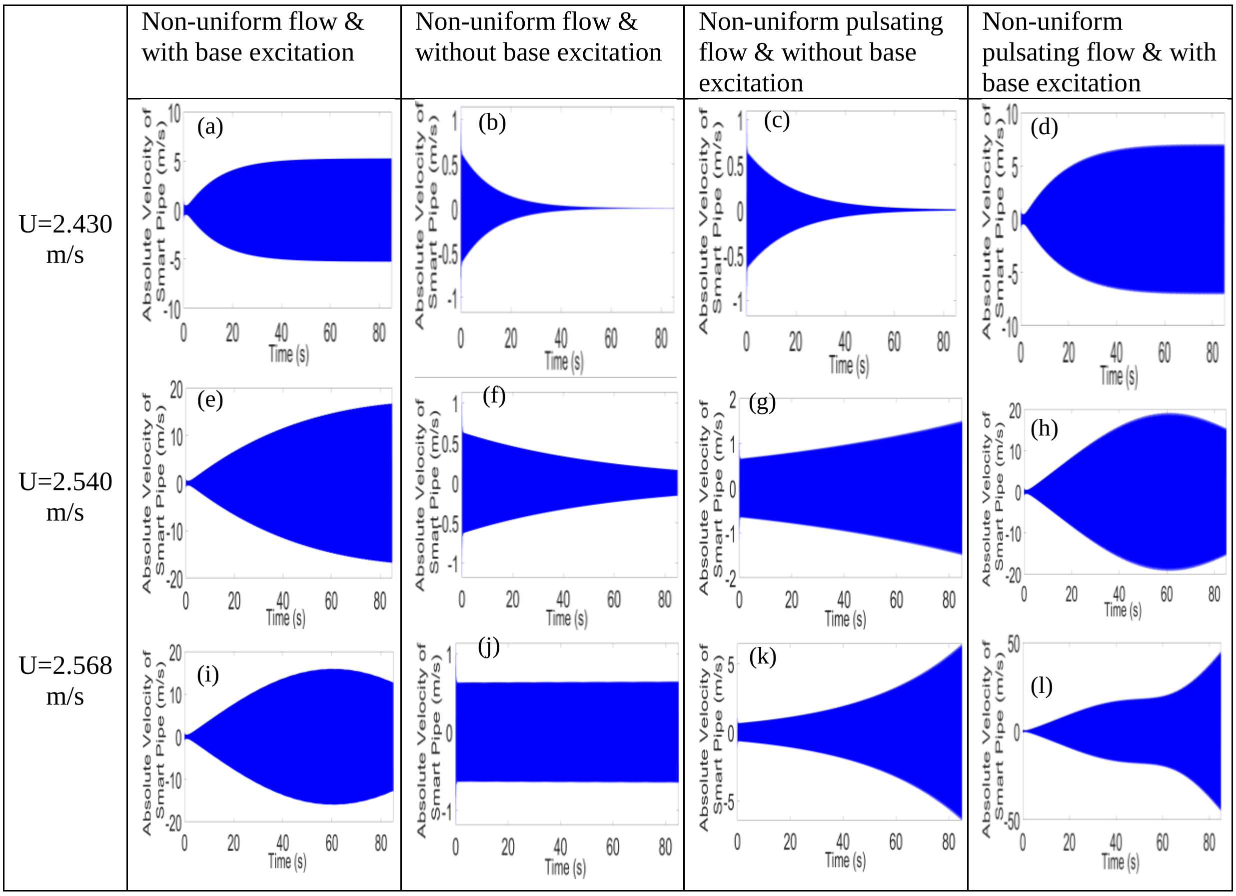

Fig.12. Evolution of the absolute velocity-time waveform of the EAP pipe under variable flow velocity using different physical parameters.

In engineering applications, the aim is to attach an energy harvesting device with a relatively small size to the main structure. For this reason, the base excitation naturally exists on the device due the vibration of the main structure itself where the related literature, as mentioned previously, has shown this essential requirement. For the smart pipe conveying fluid, a power harvesting device with a lower required flow velocity to reach the onset of the flutter instability can be developed, such as jet flow in multi-miniature elastic pipes in spacers and windsocks.

4 Conclusion

This paper has presented a theoretical approach for the partially smart pipe structure conveying fluid with non-uniform flow velocity profiles. The Navier-Stokes equations for incompressible flow for laminar and turbulent flow profiles were essentially formulated in order to determine the flow profile modification factor based on the Reynolds number and Darcy friction factor. The coupled constitutive dynamic equations for the smart pipe with the circuit interface were formulated using extended Hamiltonian mechanics. Upon considering the flow profile modification factor, the dynamic equations were further updated, giving the modified formulations. The weak form-based Ritz method analytical approach with a four-term approximation was developed to obtain the normalised dynamic equations to give the electromechanical multi-mode frequency. The numerical method used to solve the time response equations was also provided. As shown, the initial comparisons between the current method and another method for dynamic stability analysis and 3-D frequency response analysis of the smart pipe conveying ideal flow have been given, showing a good agreement. The non-ideal flow conveyed smart pipe structures using the piezoelectric ceramic and electroactive polymer material (EAP) film have been further discussed and analysed for the generation of electric power under the condition of dynamic stability and instability.

Similarly for the pipe with the two different smart materials, when the flow velocities or Reynolds numbers increased, the Darcy friction factor and flow profile modification factor decreased. As a result, for certain values of these two factors, the maximum point of the optimal power output across frequency domain occurs at the level of turbulent flow representing the critical flow velocity. In such situations, the resonance frequency shifts with increasing flow velocity until reaching the maximum point of optimal power output. Then, the optimal power output drops gradually for velocities higher than the critical flow velocity.

The pipe with the segmented piezoelectric ceramic has a single onset of flutter instability at flow velocity 4.0245 m/s and the peak resonance with power output 9.6 $mW/(m/s^2)^2$. The pipe with the segmented EAP film material has a lower critical flow velocity and can give the two peaks or maximum points of resonance of the optimal power output under variable flow velocity. This represents the occurrence of two critical flow velocities of 2.568 m/s and 13.0517 m/s. Between the two peaks, the flutter instability occurs. The stable response obviously occurs before reaching the first peak and after reaching the second peak. For the third mode, the critical flow velocity also occurs at 9.186 m/s. In this case, the instability obviously occurs between the destabilisation and restabilisation of the critical flow velocities of the second mode. This phenomenon can also be proved by the Argand diagram at the second and third modes. This can be used to control the dynamics of the smart pipe having higher flow velocity with stronger flutter. Achieving a flutter at lower flow velocity may alleviate higher responses due to the fluid flow within the smart pipe structure. The first and second onsets of the flutter instability for the second mode show optimal power outputs of 101.5 $mW/(m/s^2)^2$ and 153.6 $mW/(m/s^2)^2$, respectively. The series of dynamic time evolutions of the two physical models for the EAP pipe and piezoelectric pipe structures with variable flow velocity shows different shapes. As shown, the EAP pipe structure with the two segments evolves different shapes with wider oscillations at times where the absolute velocity gradually grows along the first segment and continues to oscillate dramatically at different levels. This indicates that the EAP pipe is more flexible than the piezoelectric pipe. This phenomenon depends on the flow velocity and the frequency of excitation, physical geometry, and material properties. The non-uniform flow pulsation and base excitation gave more pronounced effects to induce the pipe structure to generate higher power output. For engineering applications, the fluid media is not restricted to water. The fluid flow in an elastic pipe with the embedded smart material may be utilised for a power harvesting device, such as jet flow in multiple miniature elastic pipes in spacers and windsocks.

Appendix A. Stiffness coefficients for the smart pipe structure

The total transverse stiffness coefficients for the two segments located at the circumference and longitudinal regions can be formulated as,

$$C_{t1} = C_{t1}^{(1)} + C_{t1}^{(2)} = \frac{\pi \, \bar{c}_{11}^{(1)}}{2}\left(r_2^{\,4} - r_1^{\,4}\right) + \frac{\left((\beta_1 - \alpha_1) + (\beta_2 - \alpha_2)\right)\bar{c}_{11}^{(E,2)}}{4}\left(r_3^{\,4} - r_2^{\,4}\right), \quad C_{t2} = C_{t2}^{(1)} = \frac{\pi \, \bar{c}_{11}^{(1)}}{2}\left(r_2^{\,4} - r_1^{\,4}\right). \quad \text{(A.1)}$$

Appendix B. Mass moment of inertias for the smart pipe structure

The zeroth mass moment of inertias for the two segments can be formulated as

$$I_{01} = I_{t1}^{(1)} + I_{t1}^{(2)} = \pi\rho^{(1)}\left(r_2^{\,2} - r_1^{\,2}\right) + \frac{\left((\beta_1 - \alpha_1) + (\beta_2 - \alpha_2)\right)\rho^{(2)}}{2}\left(r_3^{\,2} - r_2^{\,2}\right), \quad I_{02} = C_{t2}^{(1)} = \pi\rho^{(1)}\left(r_2^{\,2} - r_1^{\,2}\right). \quad \text{(B.1)}$$

Appendix C. Transverse smart material coupling coefficient and smart material internal capacitance

The smart material couplings for the two segments can be formulated as,

$$\sigma_1 = \frac{2e_{31}^{(1)} r_3\left(r_3^{\,3} - r_2^{\,3}\right)\left(-\cos\beta_1 + \cos\alpha_1\right)}{3\left(r_3^{\,2} - r_2^{\,2}\right)}, \quad \sigma_2 = -\frac{2e_{31}^{(1)} r_3\left(r_3^{\,3} - r_2^{\,3}\right)\left(-\cos\beta_2 + \cos\alpha_2\right)}{3\left(r_3^{\,2} - r_2^{\,2}\right)}. \quad \text{(C.1)}$$

Note that the negative sign in the second part of Eq. (C1) is due to the opposite polarisation direction between the upper and lower regions of the circumference for the smart pipe. The internal capacitances can be formulated, respectively as,

$$C_{v1} = \frac{2\varepsilon_{33}^{S} r_3^{\,2} L_1(\beta_1 - \alpha_1)}{\left(r_3^{\,2} - r_2^{\,2}\right)}, \quad C_{v2} = \frac{2\varepsilon_{33}^{S} r_3^{\,2} L_1(\beta_2 - \alpha_2)}{\left(r_3^{\,2} - r_2^{\,2}\right)}. \quad \text{(C.2)}$$

Also note that the internal capacitance of the smart structure (piezoelectric component) depends on the segmented system and material properties. With the same material and segmented location, Eq. (C.2) can be used for both piezoelectric and electrode segments.

References

[1] Païdoussis, MP, Luu TP. Dynamics of a pipe aspirating fluid, such as might be used in ocean mining. ASME J Energy Resour Technol. 1985;107:250–5.

[2] Kuiper GL, Metrikine AV. Dynamic stability of a submerged, free-hanging riser conveying fluid. J Sound Vib 2005;280:1051–65.

[3] Kuiper GL, Metrikine AV. Experimental investigation of dynamic stability of a cantilever pipe aspirating fluid. J Fluids Struct 2008;24: 541–58.

[4] Païdoussis MP, Luu TP, Prabhakar S. Dynamics of a long tubular cantilever conveying fluid downwards, which then flows upwards around the cantilever as a confined annular flow. J Fluids Struct 2008; 24:111-28.

[5] Sultan G, Hemp J. Modelling of the Coriolis mass flow meter. J Sound Vib 1989;132:473-489.

[6] Xie F, Zheng X, Triantafyllou MS, Constantinides Y, Karniadakis GE. The flow dynamics of the garden-hose instability. J Fluid Mech 2016; 800: 595–612.

[7] Yoon J, Ru CQ, Mioduchowski A. Flow-induced flutter instability of cantilever carbon nanotubes. Int J Solid Struct 2006;43:3337–49.

[8] Tijsseling AS. Water hammer with fluid–structure interaction in thick-walled pipes. Comput Struct 2007;85:844–51.

[9] Kalkowski MK, Muggleton JM, Rustighi E. Axisymmetric semi-analytical finite elements for modelling waves in buried/submerged fluid-filled waveguides. Comput Struct 2018;196:327–40.

[10] Feodos'ev VP. Vibrations and stability of a pipe when liquid flows through it. Inzhenernyi Sbornik 1951;10:1013-24.

[11] Housner GW. Bending vibrations of a pipe line containing flowing fluid. J App Mech 1952;19:205-208.

[12] Niordson FI. Vibrations of a cylindrical tube containing flowing fluid. Kungliga Tekniska Hogskolans Handlingar (Stockholm) 1953;73.

[13] Long Jr RH. Experimental and theoretical study of transverse vibration of a tube containing flowing fluid. J App Mech 1955;22:65-8.

[14] Handelman GH. A note on the transverse vibration of a tube containing flowing fluid. Q Appl Math 1955;13: 326-30.

[15] Heinrich G. Schwingungen durchströmter Rohre (Vibrations of pipes with flow). Z Angew Math Mech 1956;36:417-27.
[16] Benjamin TB. Dynamics of a system of articulated pipes conveying fluid. I. Theory. Proc R Soc Lond A 1961;261:457-86.
[17] Benjamin TB. Dynamics of a system of articulated pipes conveying fluid. II. Experiments. Proc R Soc Lond A 1961;261:487-99.
[18] Gregory RW, Païdoussis MP. Unstable oscillation of tubular cantilevers conveying fluid. I. Theory Proc R Soc Lond A 1966;293:512-27.
[19] Thompson JMT. 'Paradoxical' mechanics under fluid flow. Nature 1982; 296: 135-7.
[20] Païdoussis MP, Issid NT. Dynamic stability of pipes conveying fluid. J Sound Vib 1974;33:267-94.
[21] Laithier E, Païdoussis MP. The equations of motion of initially stressed Timoshenko tubular beams conveying fluid. J Sound Vib 1981; 79:175-195.
[22] Modarres-Sadeghi Y, Païdoussis MP. Chaotic oscillations of long pipes conveying fluid in the presence of a large end-mass. Comput Struct 2013;122:192–201.
[23] Hatfield FJ, Wiggert DC, Otwell RS. Fluid-structure interaction in piping by component synthesis. ASME J Fluid Eng 1982;104:318-24.
[24] Nemat-Nasser S, Prasad SN, Herrmann G. Destability effect of velocity-dependent forces in nonconservative continuous system. AlAA J 1966;4:1276-80.
[25] Ruta GC, Elishakoff I. Towards the resolution of the Smith–Herrmann paradox. Acta Mech 2004;173:89–105.
[26] Doaré O, de Langre E. Local and global instability of fluid-conveying pipes on elastic foundations. J Fluids Struct 2002;16:1-14.
[27] Lee U, Pak CH, Hong SC. The dynamics of a piping system with internal unsteady flow. J Sound Vib 1995; 180:297–311.
[28] Gorman DG, Reese JM, Zhang YL. Vibration of a flexible pipe conveying viscous pulsating fluid flow. J Sound Vib 2000;230:379-92.
[29] Irschik H, Holl HJ. The equations of Lagrange written for a non-material volume. Acta Mech 2002;153:231–48.
[30] Stangl M, Gerstmayer M, Irschik H. An alternative approach for the analysis of nonlinear vibrations of pipes conveying fluid. J Sound Vib 2008;310:493–511.
[31] Casetta L, Pesce CP. The generalized Hamilton's principle for a non-material volume. Acta Mech 2013;224: 919–24.
[32] Païdoussis MP. Fluid–structure interactions: slender structures and axial flow, vol. 1, 2nd edn. Academic, London; 2014.
[33] De Bellis ML, Ruta GC, Elishakoff I. A contribution to the stability of an overhanging pipe conveying fluid. Contin Mech Thermodyn 2015;27:685–701.
[34] Lumentut MF, Friswell MI. A smart pipe energy harvester excited by fluid flow and base excitation. Acta Mech 2018;229:4431–58.
[35] Krommer M, Irschik H. An electromechanically coupled theory for piezoelastic beams taking into account the charge equation of electrostatics. Acta Mech 2002;154:141–58.
[36] Moita JM, Correia IFP, Soares CMM. Active control of adaptive laminated structures with bounded piezoelectric sensors and actuators. Comput Struct 2004;82:1349-58.
[37] Irschik H, Krommer M, Belyaev AK, Schlacher K. Shaping of piezoelectric sensors/actuators for vibrations of slender beams: coupled theory and inappropriate shape functions. J Intell Mater Syst Struct 1998;9:546–54.
[38] Irschik H, Krommer M, Pichler U. Dynamic shape control of beam-type structures by piezoelectric actuation and sensing. Int J Appl Electromagn Mech 2003;17:251–58.
[39] Kapuria S, Yasin MY. Active vibration control of smart plates using directional actuation and sensing capability of piezoelectric composites. Acta Mech 2013;224:1185–99.
[40] Vasques CMA. Improved passive shunt vibration control of smart piezo-elastic beams using modal piezoelectric transducers with shaped electrodes. Smart Mater Struct 2012;21:125003.
[41] Shu YC, Lien IC, Wu WJ. An improved analysis of the SSHI interface in piezoelectric energy harvesting. Smart Mater Struct 2007;16:2253–64.
[42] Goldschmidtboeing F, Woias P. Characterization of different beam shapes for piezoelectric energy harvesting. J Micromech Microeng 2008;18:104013.
[43] Dalzell P, Bonello P. Analysis of an energy harvesting piezoelectric beam with energy storage circuit. Smart Mater Struct 2012; 21:105029.
[44] Lumentut MF, Shu YC. Shunted optimal vibration energy harvesting control of discontinuous smart beams. Compos Struct 2020;242:112126.

[45] Adhikari S, Friswell MI, Inman DJ. Piezoelectric energy harvesting from broadband random vibrations. Smart Mater Struct 2009;18:115005.
[46] Ali SF, Friswell MI, Adhikari S. Piezoelectric energy harvesting with parametric uncertainty. Smart Mater Struct 2010:105010.
[47] Lumentut MF, Howard IM. Parametric design-based modal damped vibrational piezoelectric energy harvesters with arbitrary proof mass offset: numerical and analytical validations. Mech Syst Signal Process 2016; 68:562–86.
[48] Wang KF, Wang BL. An analytical model for nanoscale unimorph piezoelectric energy harvesters with flexoelectric effect. Compos Struct 2016;153:253-61.
[49] Lumentut MF, Howard IM. Intrinsic electromechanical dynamic equations for piezoelectric power harvesters. Acta Mech 2017;228:631–50.
[50] Friswell IM, Adhikari S. Sensor shape design for piezoelectric cantilever beams to harvest vibration energy. J App Phys 2010;108:014901.
[51] Lumentut MF, Howard IM. Electromechanical finite element modelling for dynamic analysis of a cantilevered piezoelectric energy harvester with tip mass offset under base excitations. Smart Mater Struct 2014;23:095037.
[52] Wu PH, Shu YC. Finite element modeling of electrically rectified piezoelectric energy harvesters. Smart Mater Struct 2015;24:094008.
[53] Lumentut MF, Shu YC. A unified electromechanical finite element dynamic analysis of multiple segmented smart plate energy harvesters: circuit connection patterns. Acta Mech 2018;229:4575-604.
[54] Lumentut MF, Shu YC. Network segmentations of smart plate structure with attached mass and dynamic motions. Eur J Mech A Solids 2021;85:104061.
[55] Lumentut MF, Francis LA, Howard IM. Analytical techniques for broadband multielectromechanical piezoelectric bimorph beams with multifrequency power harvesting. IEEE Trans Ultrason Ferroelectr Freq Control 2012;59:1555-68.
[56] Lin HC, Wu PH, Lien IC, Shu YC. Analysis of an array of piezoelectric energy harvesters connected in series. Smart Mater Struct 2013;22:094026.
[57] Wu PH, Chen YJ, Li BY, Shu YC. Wideband energy harvesting based on mixed connection of piezoelectric oscillators. Smart Mater Struct 2017;26:094005.
[58] Lumentut MF, Howard IM. Electromechanical analysis of an adaptive piezoelectric energy harvester controlled by two segmented electrodes with shunt circuit networks. Acta Mech 2017;228:1321–41.
[59] Wang J, Geng L, Ding L, Zhu H, Yurchenko D. The state-of-the-art review on energy harvesting from flow-induced vibrations. Appl Energy 2020, 267: 114902.
[60] Hobbs WB, Hu DL. Tree-inspired piezoelectric energy harvesting. J Fluids Struct 2012;28:103–14.
[61] Barrero-Gil A, Alonso G, Sanz-Andres A. Energy harvesting from transverse galloping. J Sound Vib 2010;329:2873–83.
[62] Hémon P, Amandolese X, Andrianne T. Energy harvesting from galloping of prisms: A wind tunnel experiment. J Fluids Struct 2017;70:390-402.
[63] Akcabay DT, Young YL. Hydroelastic response and energy harvesting potential of flexible piezoelectric beams in viscous flow. Phys Fluids 2012;24:054106.
[64] Michelin S, Doaré O. Energy harvesting efficiency of piezoelectric flags in axial flows. J Fluid Mech 2013;714:489–504.
[65] Hellum AM, Mukherjee R, Hull AJ. Dynamics of pipes conveying fluid with non-uniform turbulent and laminar velocity profiles. J Fluids Struct 2010; 26: 804–813.
[66] Guo CQ, Zhang CH, Païdoussis MP. Modification of equation of motion of fluid-conveying pipe for laminar and turbulent flow profiles. J Fluids Struct 2010;26: 793-803.
[67] White FM. Viscous fluid flow. 3rd ed. New York: McGraw-Hill; 2005.
[68] Durst F. Fluid mechanics: An introduction to the theory of fluid flows. Berlin Heidelberg: Springer-Verlag; 2008.
[69] Streeter VL. The kinetic energy and momentum correction factors for pipes and open channels of great width. Civil Eng ASCE 1942; 12: 212-213.
[70] Coles DE, Hirst EA. Computation of turbulent boundary layers, Proc. AFOSR-IFP, Stanford Conference 1968;2:1–45. Palo Alto, Stanford University.
[71] Haaland S. Simple and explicit formulas for the friction factor in turbulent pipe flow. ASME J Fluids Eng 1983;105:89–90.
[72] Tiersten HF. Linear piezoelectric plate vibrations. New York: Plenum; 1969.
[73] Nye JF. Physical properties of crystals: Their representation by tensors and matrices. Oxford: Clarendon; 1984.

[74] Courant R, Hilbert D. Methoden der mathematischen physik/English Ed.: Methods of mathematical physics. New York: Interscience Publishers; 1953-1962.
[75] Ritz W. Über eine neue Methode zur Lösung gewisser Variationsprobleme der mathematischen Physik. J Reine Angew Math 1909;135:1–61.